



Title	Histological analyses by matrix-assisted laser desorption/ionization-imaging mass spectrometry reveal differential localization of sphingomyelin molecular species regulated by particular ceramide synthase in mouse brains
Author(s)	Sugimoto, Masayuki; Shimizu, Yoichi; Yoshioka, Takeshi; Wakabayashi, Masato; Tanaka, Yukari; Higashino, Kenichi; Numata, Yoshito; Sakai, Shota; Kihara, Akio; Igarashi, Yasuyuki; Kuge, Yuji
Citation	Biochimica et Biophysica Acta. Molecular and Cell Biology of Lipids, 1851(12), 1554-1565 <a href="https://doi.org/10.1016/j.bbalip.2015.09.004">https://doi.org/10.1016/j.bbalip.2015.09.004</a>
Issue Date	2015-12
Doc URL	<a href="http://hdl.handle.net/2115/63713">http://hdl.handle.net/2115/63713</a>
Rights	© 2015. This manuscript version is made available under the CC-BY-NC-ND 4.0 license <a href="http://creativecommons.org/licenses/by-nc-nd/4.0/">http://creativecommons.org/licenses/by-nc-nd/4.0/</a>
Rights(URL)	<a href="http://creativecommons.org/licenses/by-nc-nd/4.0/">http://creativecommons.org/licenses/by-nc-nd/4.0/</a>
Type	article (author version)
File Information	Manuscript.pdf



[Instructions for use](#)

**Histological analyses by matrix-assisted laser desorption/ionization-imaging mass spectrometry reveal differential localization of sphingomyelin molecular species regulated by particular ceramide synthase in mouse brains**

Masayuki Sugimoto<sup>a,b</sup>, Yoichi Shimizu<sup>c</sup>, Takeshi Yoshioka<sup>a</sup>, Masato Wakabayashi<sup>a</sup>, Yukari Tanaka<sup>d</sup>, Kenichi Higashino<sup>a</sup>, Yoshito Numata<sup>a</sup>, Shota Sakai<sup>e</sup>, Akio Kihara<sup>f</sup>, Yasuyuki Igarashi<sup>c</sup>, and Yuji Kuge<sup>b,c,\*</sup>

<sup>a</sup>Shionogi Innovation Center for Drug Discovery, Discovery Research Laboratory for Innovative Frontier Medicines, Shionogi & Co., Ltd., Sapporo 001-0021, Japan

<sup>b</sup>Department of Integrated Molecular Imaging, Graduate School of Medicine, Hokkaido University, Sapporo 060-0815, Japan

<sup>c</sup>Central Institute of Isotope Science, Hokkaido University, Sapporo 060-0815, Japan

<sup>d</sup>Shionogi Pharmacological Research Center, Research Laboratory for Development, Shionogi & Co., Ltd., Osaka 561-0825, Japan

<sup>e</sup>Department of Biomembrane and Biofunctional Chemistry, Faculty of Advanced Life Science, Hokkaido University, Sapporo 001-0021, Japan

<sup>f</sup>Department of Biochemistry, Faculty of Pharmaceutical Science, Hokkaido University, Sapporo 060-0812, Japan

\*To whom correspondence should be addressed:

Central Institute of Isotope Science, Hokkaido University, Kita-15-jo, Nishi 7-chome,

Kita-ku, Sapporo 060-0815, Japan

Tel: +81-11-706-6088

Fax: +81-11-706-7862

E-mail: kuge@ric.hokudai.ac.jp

### **Abbreviations**

SM, sphingomyelin; SMS, sphingomyelin synthase; Cer, ceramide; CerS, ceramide synthase; LC/ESI-MS/MS, liquid chromatography/electrospray ionization-tandem mass spectrometry; IMS, imaging mass spectrometry; ISH, *in situ* hybridization; MALDI, matrix-assisted laser desorption/ionization; FTICR, Fourier transform ion cyclotron resonance; VLCFA, very long-chain fatty acid; HexCer, hexosylceramide; GlcCer, glucosylceramide; GalCer, galactosylceramide; LacCer, lactosylceramide

## **Abstract**

Sphingomyelin (SM) is synthesized by SM synthase (SMS) from ceramide (Cer). SM regulates signaling pathways and maintains organ structure. SM comprises a sphingoid base and differing lengths of acyl-chains, but the importance of its various forms and regulatory synthases is not known. It has been reported that Cer synthase (CerS) has restricted substrate specificity, whereas SMS has no specificity for different lengths of acyl-chains. We hypothesized that the distribution of each SM molecular species was regulated by expression of the CerS family. Thus, we compared the distribution of SM species and CerS mRNA expression using molecular imaging. Spatial distribution of each SM molecular species was investigated using ultra-high-resolution imaging mass spectrometry (IMS). IMS revealed that distribution of SM molecular species varied according to the lengths of acyl-chains found in each brain section. Furthermore, a combination study using *in situ* hybridization and IMS revealed the spatial expression of CerS1 to be associated with the localization of SM (d18:1/18:0) in cell body-rich gray matter, and CerS2 to be associated with SM (d18:1/24:1) in myelin-rich white matter. Our study is the first comparison of spatial distribution between SM molecular species and CerS isoforms, and revealed their distinct association in the brain. These observations were demonstrated by suppression of CerS2 using siRNA in HepG2 cells; that is, siRNA for CerS2 specifically decreased C22 very long-chain fatty acid (VLCFA)- and C24 VLCFA-containing SMs. Thus, histological analyses of SM species by IMS could be a useful approach to consider their molecular function and regulative mechanism.

**Keywords**

Imaging mass spectrometry; Fourier-transform ion cyclotron resonance; Sphingomyelin;  
Ceramide synthase; Very long-chain fatty acid

## 1. Introduction

Sphingolipids have important roles in the stabilization of membrane structures, and are signaling molecules [1–4]. Sphingomyelin (SM), which is the final product of the synthesis of sphingolipids, is a signaling regulator [5–7]. SM has also been reported to be involved in certain diseases. Niemann–Pick disease is a genetically inherited disease caused by a deficiency in sphingomyelinase, which causes accumulation of SM in some organs (e.g., liver, lungs, brain) and results in irreversible neurologic damage [6]. Additionally, a deficiency of sphingomyelin synthase 2 (SMS2) ameliorates diet-induced obesity, fatty liver disease, and insulin resistance [8–10].

Sphingolipids contain ceramide (Cer) as a backbone, in which a fatty acid (FA) is amide-linked to the sphingoid base (Sph). Most saturated and monounsaturated very long-chain fatty acids (VLCFAs) are found as acyl groups in sphingolipids. The *de novo* synthesis of sphingolipids begins in the endoplasmic reticulum (ER) with the conversion of L-serine and palmitoyl-CoA into Cer. These reactions are mediated by serine palmitoyltransferase, 3-ketosphinganine reductase, Cer synthase (CerS), and dihydroceramide desaturase 1 [11–13]. As a precursor of SM, part of Cer molecules is transferred from the ER to the Golgi by Cer transport protein [14, 15]. In the Golgi, Cer is converted to SM or glucosylceramide (GlcCer) and subsequently to lactosylceramide (LacCer) by SMS or UDP-glucose ceramide glucosyltransferase (Ugcg), respectively [16–19]. SM is synthesized from Cer by the transfer of phosphocholine (PCho) from phosphatidylcholine through SMS1 in the Golgi or SMS2 in plasma membranes [16, 17,

20].

Even though reports showing which SMS has specificity for different lengths of the acyl-chains of Cer are lacking, it is known that formation of an amide bond between acyl-CoA and the Sph is catalyzed by CerS [21, 22]. Six CerS isoforms (CerS1–CerS6) have been identified and each one exhibits restricted substrate specificity to FAs with specific chain lengths [21–23]. For example, CerS1 is primarily responsible for the synthesis of C18 long-chain fatty acid (LCFA)-containing sphingolipids [24], whereas CerS2 is responsible for the synthesis of C22–C24 VLCFA-containing sphingolipids [25–28]. It has also been shown that CerS exhibits ubiquitous or tissue-specific distribution patterns [23]. For example, CerS1 is specifically expressed in the brain and skeletal muscle, whereas CerS2 is ubiquitously expressed in most tissues, in particular in the liver and kidneys [23]. Thus, the tissue-distribution patterns of Cer molecular species could be identified according to their substrate specificity.

FA compositions of SM range mainly from C16 to C24; C16:0, C24:0 and C24:1 FA-containing SMs are major components in most mammalian tissues [23]. However, the proportion of each FA among tissues varies considerably. For example, C24 VLCFAs are major components of SM in the liver and kidneys, whereas C18 LCFAs are major components of SM in the brain and skeletal muscle [23]. It has been reported that the FA composition of sphingolipids is markedly dependent on the cell types in each organ [24, 28]. Neurons synthesize mainly C18 LCFA-containing sphingolipids [24], whereas

oligodendrocytes and Schwann cells (which wind tightly around axons to form myelin sheaths) mostly synthesize C24 VLCFA-containing sphingolipids [28]. Thus, clarifying the spatial information for SM is important to understand the properties of SM and the functions or distributions of cells within tissue because each type of cell has different SM species. However, few reports have identified the distribution of each molecular species of SM, or compared SM and its distribution pattern of regulatory synthases, by histologic means.

Liquid chromatography/electrospray ionization-tandem mass spectrometry (LC/ESI-MS/MS) is the “gold standard” method for the measurement of lipids within tissues. However, histologic information is lost by the extraction procedure. Matrix-assisted laser desorption/ionization-imaging mass spectrometry (MALDI-IMS) is expected to be a powerful tool to visualize the distribution of various molecules (including lipids) in tissue sections [29–33]. Several reports have shown that MALDI-IMS can be used for imaging of the sites of endogenous metabolites, especially glycerophospholipids and sphingolipids [34–38]. Furthermore, use of MS/MS allows the structures of imaged molecules to be identified [39, 40]. Comparison of the distribution of lipid molecules and expression of their synthases would likely clarify their relationship, but no studies have compared them directly. However, it has been stated that conventional MALDI-time of flight-mass spectrometry (TOF-MS) cannot be employed for the identification of endogenous metabolites (including lipids) because very close mass peaks are often observed as a single overlapping peak owing to low mass resolution [41]. These limitations make identification

of each peak in IMS by MS/MS very difficult. Conversely, Fourier transform ion cyclotron resonance-mass spectrometry (FTICR-MS) can be used to specifically identify the exact mass and isotopic fine structure of each molecule by its ultra-high-resolution [34, 42, 43]. Thus, MALDI-FTICR-IMS enables scholars to distinguish between structurally heterogeneous molecules according to their exact mass and to visualize them simultaneously.

Thus, the aims of this study were first to determine whether SM was differently distributed by its acyl-chain lengths, and second, to compare the distributions of SM with the expression patterns of CerS in the brain by employing MALDI-IMS of lipids and *in situ* hybridization (ISH) of metabolizing genes.

## 2. Materials and methods

### 2.1. Materials

High-performance liquid chromatography-grade methanol, acetonitrile, chloroform, n-hexane and 2-propanol were purchased from Kanto Chemical Co., Inc. (Tokyo, Japan). Trifluoroacetic acid, ammonium acetate, potassium acetate, potassium hydroxide and hydrochloric acid were obtained from Wako Pure Chemical Co., Ltd. (Osaka, Japan). 2,5-dihydroxybenzoic acid (DHB) and formic acid were purchased from Sigma–Aldrich (Saint Louis, MO). Indium tin oxide (ITO) glass slides were obtained from Bruker Daltonics (Bremen, Germany). Complete Protease Inhibitor Cocktail was purchased from Roche Diagnostics (Basel, Switzerland).

SM (d18:1/16:0), SM (d18:1/18:0), SM (d18:1/18:1), SM (d18:1/24:0), SM (d18:1/24:1), SM (d18:1/16:0-d31), Cer (d18:1/16:0), Cer (d18:1/18:0), Cer (d18:1/18:1), Cer (d18:1/22:0), Cer (d18:1/24:0), Cer (d18:1/24:1), Cer (d18:1/16:0-d31), GalCer (d18:1/24:1) and LacCer (d18:1/18:0) standards were purchased from Avanti-Polar Lipids Inc. (Alabaster, AL). Trizol RNA Separation Reagent and the SuperScript III First-Strand Synthesis system for reverse transcription-polymerase chain reaction (RT-PCR) were obtained from Life Technologies (Carlsbad, CA). An RNeasy Mini Kit was purchased from Qiagen (Venlo, the Netherlands). SYBR Premix Ex Taq II and Perfect Real Time Primer were obtained from Takara Bio Inc. (Otsu, Japan).

Silencer Select Negative Control siRNA, Pre-designed siRNA, Opti-MEM and Lipofectamine RNA iMAX Transfection Reagent were purchased from Life Technologies. Dulbecco's Modified Eagle's Medium (DMEM) containing glucose (1.0 mg/mL) was obtained from Nacalai Tesque (Suita, Japan). Fetal bovine serum was purchased from GE Healthcare Life Sciences (Logan, Utah). Lipoprotein-depleted serum (LPDS) was obtained from Sigma–Aldrich. Micro BCA Assay Reagent was purchased from Thermo Fisher Scientific Inc. (Waltham, MA). Cell Lysis Buffer was obtained from Cell Signaling Technology, Inc. (Danvers, MA).

## 2.2. *Animals*

The animal research protocol was approved by the Animal Care and Use Committee of the Graduate School of Medicine, Hokkaido University (Sapporo, Japan). The protocol conformed to the *Guide for the Care and Use of Laboratory Animals* (US National Institutes of Health, Bethesda, MD).

Male C57BL/6N mice were purchased from CLEA Japan Inc. (Tokyo, Japan). Mice (age, 4 weeks) were housed in separate cages under controlled temperature and humidity with a 12 h light–dark cycle for 1 week. Tissues were removed from 5 weeks of age under isoflurane anesthesia after 4 h of fasting and weighed. They were snap-frozen on dry ice, and stored at  $-80^{\circ}\text{C}$  until analyses.

## 2.3. *Culture and transfection of cells*

HepG2 cells were maintained in culture medium (DMEM supplemented with 10% fetal bovine serum and 1% antibiotic–antimycotic (100 ×) liquid), and cultured at 37°C in an atmosphere of 5% CO<sub>2</sub>. Lipofectamine RNA iMAX Transfection Reagent and Silencer Select siRNA (Negative Control Number 1, part number: 4390843; Negative Control Number 2, part number: 4390846; CerS2 Number 1, part number: 4427037, ID: s26788; CerS2 Number 2, part number: 4427037, ID: s26789; SMS2 Number 1, part number: 4392420, ID: s46645; SMS2 Number 2, part number: 4392420, ID: s46646) were diluted in Opti-MEM. Diluted siRNA were added to diluted Lipofectamine RNA iMAX Transfection Reagent (1:1, v/v) and incubated at room temperature for 5 min. Cells were seeded in 24-well plates at  $1 \times 10^5$  cells per well and added to siRNA–lipid complex (1.2 pmol of siRNA and 1 μL of Lipofectamine RNA iMAX Transfection Reagent per well). Cells were incubated for 6 h and the medium was changed. 24 h after transfection, cells were cultured in DMEM supplemented with 10% LPDS for 72 h.

#### *2.4. Lipid extraction for lipid measurement*

Total lipids were extracted from animal tissues according to a modified method of Bligh and Dyer [44]. Briefly, snap-frozen tissues (50 mg) were freeze-dried and homogenized in 0.5 mL of saline supplemented with protease inhibitor cocktail. To 50 μL of homogenate, 400 μL of water was added, followed by extraction with 1 mL of chloroform/methanol (1:1, v/v) solution containing 50 ng/mL of internal standards. The internal standards used were stable isotopes of SM and Cer, SM (d18:1/16:0-d31) and Cer (d18:1/16:0-d31). After centrifugation, the lower organic phase was collected. A total of 500 μL of

chloroform/methanol (2:1, v/v) was added to the upper aqueous phase. After centrifugation, the lower organic phase was collected and combined with the first organic phase that had been collected. Extracts were dried under nitrogen, reconstituted in 500  $\mu$ L of chloroform/methanol (1:1, v/v), and saponified with 6  $\mu$ L of 8 N KOH for 2 h at 37°C. After saponification, the extract was naturalized with 180  $\mu$ L of 0.67 N HCl and centrifuged. After centrifugation, the lower organic phase was collected and 500  $\mu$ L of chloroform/methanol (2:1, v/v) was added to the upper aqueous phase. After centrifugation, the lower organic phase was collected and combined with the first organic phase that had been collected. After drying under nitrogen, it was reconstituted in 400  $\mu$ L of chloroform/methanol/H<sub>2</sub>O (50:400:50, v/v).

Total lipids were also extracted from cells, as described previously [45]. Briefly, 300  $\mu$ L of 2-propanol containing 50 ng/mL of internal standard was added to the wells. Extracts were collected after scraping with a Teflon cell scraper. Collected extracts were added to 900  $\mu$ L of n-hexane. Wells were rinsed with 300  $\mu$ L of 2-propanol, which was combined with the extracts. After centrifugation, the organic phase was collected and dried under nitrogen, and reconstituted in 330  $\mu$ L of chloroform/methanol/H<sub>2</sub>O (50:400:50, v/v). Residual pellets were dried overnight at room temperature and dissolved in 100  $\mu$ L of cell lysis buffer. After centrifugation, supernatants were removed for protein determination by the BCA assay, which was performed according to the manufacturer's protocol.

### *2.5. Lipid measurement by LC/ESI-MS/MS*

LC/ESI-MS/MS analyses were carried out according to the methods described by Sanaki (personal communication) using UltiMate 3000 HPLC (Thermo Fisher Scientific Inc.) and a Q Exactive Plus Hybrid Quadrupole-Orbitrap Mass Spectrometer (Thermo Fisher Scientific Inc.). Briefly, lipid extracts were separated with an ACQUITY UPLC BEH C18 column (1.7  $\mu\text{m}$ , 2.1  $\times$  100 mm; Waters Co., Milford, MA). Then, 4  $\mu\text{L}$  of sample was injected. The oven temperature of the column was set at 60°C. Conditions for the mobile phase were: linear gradient analyses with mobile phase A (H<sub>2</sub>O with 1% ammonium acetate, 0.1% formic acid, 0.00005% phosphate), and mobile phase B (50% acetonitrile, 50% 2-propanol, 1% ammonium acetate, 0.1% formic acid) at a flow rate of 0.4 mL/min. The gradient program was as follows: 0–43 min (B 50%), 43–48 min (B 100%), 48–50 min (B 50%). Measurement of lipid levels was undertaken in positive ion mode. MS spectra were obtained by full scan mode. Data-dependent MS/MS (ddMS<sup>2</sup>) spectra were obtained by MS/MS mode. MS spectra were acquired under operator control with target mass resolution of  $R = 70,000$  at  $m/z$  200, and the scan range set at  $m/z$  200–1,300. ddMS<sup>2</sup> spectra were also acquired with a target mass resolution of  $R = 17,500$  at  $m/z$  200, and the scan range was set at  $m/z$  200–2,000. The automatic gain control (AGC) target of MS was set to  $1 \times 10^6$  and the maximum injection time (IT) of MS was set to 100 ms. The AGC target of ddMS<sup>2</sup> was set to  $5 \times 10^4$  and the maximum IT of ddMS<sup>2</sup> was set to 50 ms. Heated-ESI parameters were set as follows: sheath gas flow rate, 50 units; auxiliary gas flow rate, 13 units; ion spray voltage, 3.80 kV; ion transfer capillary temperature, 350°C; and auxiliary gas heater temperature, 425°C. Stepped normalized collision energy was set to 25, 35 and 45 eV.

Lipid identification was undertaken using Lipid Search software (Mitsui Knowledge Industry Co., Ltd., Tokyo, Japan), as described previously [46]. In the present study, the parent search mode and product search mode were used. Precursor tolerance was set to 5 ppm mass window and the product tolerance was set to 8 ppm mass window. The relative intensity threshold of product ions was set to 1%. The *m*-score threshold was set to 5.0. Target lipids in the present study were identified to be  $[M+H]^+$ ,  $[M+Na]^+$  and  $[M+NH_4]^+$ .

#### *2.6. Sample preparation for MALDI-IMS*

Frozen tissues were sectioned at  $-16^{\circ}\text{C}$  using a CM3050 Cryostat (Leica, Solms, Germany) to a thickness of 10  $\mu\text{m}$ . Frozen sections were mounted on ITO glass slides for IMS analyses. A DHB solution (30 mg/mL DHB, 20 mM potassium acetate, 50% MeOH, 0.2% trifluoroacetic acid) was used as the matrix solution, as described previously [35]. The matrix solution was sprayed onto sections using Image Prep (Bruker Daltonics).

#### *2.7. MALDI-IMS*

MALDI-FTICR-IMS analyses were conducted using a 7T solariX XR system (Bruker Daltonics). To detect lipid species, the continuous accumulation of selected ions (CASI) function was used in positive ion mode over a mass range  $m/z$  500–900 with a resolution of 590,000 at  $m/z$  400. A Smart Beam II laser was operated at 2,000 Hz, a laser power of 50%, a laser diameter of 50  $\mu\text{m}$ , and a raster width of 80  $\mu\text{m}$ . The SM peak obtained was accumulated and split by collision-induced dissociation (CID)-fragmentation with CASI function to obtain structural information. Mass spectra were analyzed and obtained using

Data Analysis v4.3 (Bruker Daltonics).

MALDI-TOF-IMS analyses were undertaken using ultrafleXtreme (Bruker Daltonics). To detect lipid species, a reflector positive mode was used over a mass range  $m/z$  0–1,000. A Smart Beam II laser was operated at 2,000 Hz, a laser power of 80%, a laser diameter of 100  $\mu\text{m}$ , and a raster width of 100  $\mu\text{m}$ . Mass spectra were analyzed and obtained using FlexAnalysis v3.3 (Bruker Daltonics).

After acquisition of mass spectra, FlexImaging v4.0 (Bruker Daltonics) was used for data processing and image generation. All imaging data were normalized by the root means square method. Lipid identification was undertaken using the MS analysis tool in the LIPID MAPS website ([www.lipidmaps.org/tools/index.html](http://www.lipidmaps.org/tools/index.html)).

#### *2.8. RNA extraction and real-time PCR*

Total RNA was extracted using Trizol Reagents and an RNeasy Mini kit according to the manufacturer's protocol. Reverse transcription was done using a SuperScript III First-Strand Synthesis system for RT-PCR and PCR Thermal Cycler SP (Takara Bio Inc.). Real-time PCR was carried out using SYBR Premix Ex Taq II, Perfect Real Time Primer (Table S1) and a 7500 Real-time PCR system (Life Technologies).

#### *2.9. ISH*

ISH was performed by Ourgenic Co., Ltd. (Naruto, Japan). For ISH in tissue, brains were

rapidly frozen in dry-ice powder, cut into 10  $\mu\text{m}$  sections and mounted on positively charged glass slides. A commercially available mRNA ISH kit (QuantiGeneViewRNA, Panomics Inc., Fremont, CA) was used according to the manufacturer's protocol. Mouse-CerS1-specific probe (accession number NM\_138647, 134–1,299 nt) and Mouse-CerS2-gene-specific probe (NM\_029789, 36–1,337 nt) were designed and synthesized by Panomics/Affymetrix. To design and synthesize the specific probe, the specificity of each oligonucleotide was determined using the BLAST database (<http://blast.ncbi.nlm.nih.gov/Blast.cgi>) and screened *in silico*. The “ZZ” method (which requires two oligonucleotides to be paired up to produce a signal) was also used. Probe sets and amplifier molecules were hybridized to each pair of oligonucleotides. Alkaline phosphatase was used to break down the fast red substrate to form precipitates. Images of the hybridized target mRNA were acquired by using a BIOREVO BZ-9000 imaging microscope and image joint software (Keyence, Osaka, Japan). ISH of glyceraldehyde 3-phosphate dehydrogenase (GAPDH) was performed as a positive control, and ISH without probes was performed as a negative control for the study of brain sections (Fig. S1A and B).

### 2.10. Histology

The morphology of brain tissue was observed through routine slicing, and hematoxylin and eosin (H&E) and Kluver–Barrera (KB) staining. For H&E staining, sections were fixed with 10% formamide, stained with Mayer's hematoxylin for 5 min, rinsed with H<sub>2</sub>O and stained with Eosin Y for 1 min. For KB staining, sections were hydrated with 95% ethanol,

stained in 0.1 % Luxol Fast-Blue (LFB) for 12 h at 60°C, and rinsed with 70% ethanol and 0.1 % Cresyl-Violet (CV) for 5 min. All procedures were performed by Ourgenic Co., Ltd. Preparation of virtual slides as well as addition of the names and boundaries of the specific regions of the brain section were performed by Biopathology Institute Co., Ltd. (Kunisaki, Japan).

### *2.11. Statistical analyses*

Experimental values are the mean  $\pm$  SD. Statistical analyses were carried out by Dunnett's multiple comparison test using SAS v9.2 (SAS Institute, Cary, NC).  $p < 0.05$  was considered significant.

### 3. Results

#### *3.1. Composition of SM and Cer and expression of CerS family members in mouse brain*

We first performed structural analyses of SM by MS/MS using LC/ESI-MS/MS to determine the lengths of Sph and acyl-chains of SM. Product ions [PCho+H]<sup>+</sup> (*m/z* 184.0733) corresponding to PCho, and [Sph (d18:1)-2H<sub>2</sub>O+H]<sup>+</sup> (*m/z* 264.2686) corresponding to d18:1 Sph, were obtained from the parent ion [SM (36:1)+H]<sup>+</sup> (*m/z* 731.6061) (Fig. S2A–C). However, the product ion [Sph (d20:1)-2H<sub>2</sub>O+H]<sup>+</sup> (*m/z* 292.2999) corresponding to d20:1 Sph, was not observed. We also performed the structural analyses of LacCer as the reference lipid. [Sph (d20:1)-2H<sub>2</sub>O+H]<sup>+</sup> (*m/z* 292.2999) was obtained from the parent ion [LacCer (38:1)+H]<sup>+</sup> (*m/z* 918.6876) (Fig. S2A–C). Product ion [Sph (d18:1)-2H<sub>2</sub>O+H]<sup>+</sup> (*m/z* 264.2686) was also observed from the parent ion [LacCer (36:1)+H]<sup>+</sup> (*m/z* 890.6563) (Fig. S2A–C). Next, we determined SM and Cer compositions in lipid extracts from the forebrain and cerebellum using a LC/ESI-MS/MS system. Major components in the forebrain and cerebellum were SM (d18:1/18:0) and SM (d18:1/24:1) (Fig. 1A and B). Furthermore, major components of the Cer family included Cer (d18:1/18:0) and Cer (d18:1/24:1) in the forebrain and cerebellum (Fig. 1C and D). We also determined the expression of CerS mRNA in the forebrain and cerebellum. Consistent with the concentrations of SM (d18:1/24:1) and Cer (d18:1/24:1), CerS2 (which is responsible for the synthesis of C22–C24 VLCFA-containing sphingolipids) was expressed in these tissues. Importantly, CerS1 (which is responsible for the synthesis of C18 LCFA-containing sphingolipids) was also expressed in the brain, as were distributions of Cer (d18:1/18:0)

and SM (d18:1/18:0) (Fig. 1E and F).

### *3.2. Detection and characterization of SM by MALDI-FTICR-IMS*

We revealed different SM profiles in the brain, but histologic information was not clear. Therefore, we evaluated the distribution pattern of each SM molecular species in the brain using MALDI-FTICR-IMS. First, we obtained mass spectra from sphingolipid standards, i.e., SM (d18:1/16:0), SM (d18:1/18:0), SM (d18:1/18:1), SM (d18:1/24:0), SM (d18:1/24:1) and galactosylceramide (GalCer) (d18:1/24:1) on ITO glass slides using the positive ion detection mode of MALDI-FTICR-IMS (Fig. S3A–C). Using the spectra for standards, structural analyses by CID fragmentation on ITO glass slides was carried out (Fig. S4A–E). A PCho head group was confirmed by neutral losses of 59 u and 183 u from precursor ions. Next, we evaluated mass spectra in the range  $500 < m/z < 900$  from sections of mouse forebrains (Fig. 2B–E). Six mass peaks were assigned to SM molecular species as potassium adducts, and two mass peaks were assigned to hexosylceramide (HexCer) as a potassium adduct, using their exact mass values (Fig. S5A–F). Among them, five mass peaks were also validated by comparison with the mass spectra obtained from sphingolipid standards. These assignments of SM were also confirmed with structural analysis of each peak by CID fragmentation in tissue (Fig. S6A–D). As seen with the standards, a PCho head group was confirmed by neutral losses of 59 u and 183 u from precursor ions (Figs. S4 and S6).

### *3.3. Visualization of SM in forebrain sections by MALDI-IMS*

We evaluated the site of each SM molecular species in two coronal regions of the brain. A different distribution pattern was observed in the forebrain, which contains the hippocampus (Hip) and hypothalamus (Hy). Very low concentrations of SM (d18:1/16:0) and SM (d18:1/22:0) were observed in the LC/ESI-MS/MS study in homogenates of forebrain tissue (Fig. 1A). However, MALDI-FTICR-IMS revealed the specific distribution pattern of SM (d18:1/16:0) (Figs. 2B and 3A) and SM (d18:1/22:0) (Figs. 2D and 3D) in the lateral ventricle (LV), third ventricle (3V) and dorsal third ventricle (D3V). SM (d18:1/18:0) was distributed widely in the gray matter (GM) of the forebrain, including the Hip, Hy, caudate putamen (CPu) and cerebral cortex (Cx) (Figs. 2C and 3B). The SM (d18:1/18:1) level was very low, but distributed generally in the Hip, Hy, CPu and Cx (Figs. 2C and 3C). In contrast to SM (d18:1/18:0), two VLCFA-containing SMs, SM (d18:1/24:0) and SM (d18:1/24:1), were localized specifically in the white matter (WM) or in the region containing the myelin sheath in the forebrain, including the thalamus (Tha), internal capsule (IC), corpus callosum (CC) and fimbria hippocampi (Fi) (Figs. 2E, 3E and F). HexCer (d18:1/24:1) was also distributed in the WM as well as SM (d18:1/24:0) and SM (d18:1/24:1) (Figs. 2E and 3G). We also visualized the distribution of each SM species in forebrain sections by MALDI-TOF-IMS (Figs. S7 and S8). Even though their spatial resolutions and obtained signals were lower than the results of MALDI-FTICR-IMS, similar distribution patterns were observed for each SM species. These results were obtained from three individuals.

#### *3.4. Visualization of SM localization in cerebellum sections by MALDI-IMS*

Next, we evaluated the distribution of each SM molecular species in the cerebellum. Similar to the forebrain, SM (d18:1/16:0) (Figs. 4B and 5A) and SM (d18:1/22:0) (Figs. 4D and 5D) were highly distributed in the fourth ventricle (4V) in the cerebellum. SM (d18:1/18:0) was distributed widely in the GM, including the molecular layer (ML), granule cell layer (GCL) and Purkinje cell layer (PCL) of the cerebellum (Figs. 4C and 5B), whereas SM (d18:1/24:0) and SM (d18:1/24:1) were localized specifically in the WM and myelin sheath-rich region of the cerebellum and medulla (Md) (Figs. 4E, 5E and F). HexCer (d18:1/24:1) was also distributed in the region where SM (d18:1/24:0) and SM (d18:1/24:1) were distributed in the cerebellum (Figs. 4E and 5G). These results were obtained from three individuals.

### *3.5. Comparison of SM localization and CerS expression in brain sections*

We next compared the histologic distribution of CerS with each SM molecular species in sagittal sections of brain tissue to clarify the mechanism underlying these distinct spatial distributions of SM. KB staining revealed that Nissl bodies (which are commonly present in neurons but less so in axons) were stained by CV (as shown by black arrowheads in Fig. 6C), and myelin (which is present in axons) was stained by LFB (as shown by white arrowheads in Fig. 6B and C). In addition to the results for coronal sections, SM (d18:1/18:0) was distributed widely in the GM of the GCL, Hip, Hy, CPu, anterior olfactory nucleus (AO), ventral striatum (VS), substantia nigra (SN) and Cx (Fig. 6F), whereas SM (d18:1/24:1) was localized specifically in the LFB-positive WM, including the WM of the cerebellum, CC, Fi, midbrain (Mb), pons (Pn), Md, anterior commissure (AC) and optic

tract (OT) (as shown by arrowheads in Fig. 6G). Interestingly, CerS2 expression was strongly detected in the WM, including the WM of the cerebellum, CC, Fi, AC and OT, as well as SM (d18:1/24:1) (as shown by arrowheads in Fig. 6E). Expression of CerS1 was markedly different to that of CerS2. Prominent expression of CerS1 was detected in the GM, including the GCL, Hip, Hy, Cx, CPu, AO, VS and SN, similar to that seen for SM (d18:1/18:0), whereas it was less expressed in the WM (as shown by arrowheads in Fig. 6D). These results were obtained from two individuals.

### *3.6. Responses of each SM molecular species to CerS2 and SMS2 suppression in HepG2 cells*

To verify our observations, we evaluated the responses of each SM species to CerS2 suppression in HepG2 cells (CerS2 is highly expressed in HepG2 cells and prefers only C22–C24 VLCFAs, whereas other CerS isoforms prefer C16–C18 LCFAs). Two different kinds of siRNAs for CerS2 markedly decreased CerS2 expression compared with negative control siRNA in HepG2 cells (Fig. 7A). As expected, these siRNAs for CerS2 specifically decreased C22 and C24 VLCFA-containing SMs compared with negative control siRNA in HepG2 cells (Fig. 7B). We also evaluated the effect of SMS2 suppression on the composition of SM in HepG2 cells (SMS2 is highly expressed in HepG2 cells and shows no substrate specificity for the lengths of the acyl-chains of Cer). Two different kinds of siRNAs for SMS2 markedly decreased SMS2 expression compared with negative control siRNA in HepG2 cells (Fig. 7C). Furthermore, in contrast to CerS2, these siRNAs for SMS2 universally decreased SM species compared with negative control siRNA in HepG2

cells (Fig. 7D).

#### 4. Discussion

In the present study, we investigated the distribution of SM species using MALDI-FTICR-IMS and compared it with the expression of CerS gene in brain sections. Distribution of SM species was different according to the lengths of their acyl-chains and correlated with the expression of particular CerS. Collectively, these results indicate an important role for CerS in the distribution of SM and maintenance of the structure and function of particular organs.

We undertook a histologic study of SM using MALDI-IMS because MALDI-IMS is expected to be a powerful tool for the visualization of lipids, which are difficult to detect by immunohistochemical analyses. However, it has been stated that conventional MALDI-TOF-IMS cannot be employed for the identification of endogenous metabolites (including lipids) because very close mass peaks are often observed as a single overlapping peak owing to low mass resolution [41]. These limitations make identification of each peak in IMS by MS/MS very difficult.

In contrast to MALDI-TOF-IMS, ultra-high-resolution MALDI-FTICR-IMS can be used to directly identify each peak by its exact mass and isotopic fine structure [34, 42]. Very close mass peaks can be separated clearly and visualized as independent images by MALDI-FTICR-IMS [43]. Here, we also compared MALDI-TOF-IMS with MALDI-FTICR-IMS for imaging where SM is located (Figs. 2, 3, S7 and S8). In the MALDI-TOF-IMS study, a single peak was identified at  $m/z$  825.6, 851.6 and 853.6, and

these peaks were assigned to SM (d18:1/22:0), SM (d18:1/24:1) and SM (d18:1/24:0), respectively (Fig. S8C and D). However, the peak assigned to each  $m/z$  by MALDI-TOF-IMS was separated into other peaks and identified specifically in the MALDI-FTICR-IMS study because of its ultra-high-resolution (Fig. S5C–F). As a result, MALDI-FTICR-IMS enabled us to obtain very highly specific and sensitive spatial information for SM. Thus, MALDI-FTICR-IMS could be a powerful tool to visualize the sites of various endogenous molecules in tissue sections.

We identified each SM molecular species by its exact mass and neutral losses of product ions, PCho, from precursor ions using MALDI-FTICR-IMS (Figs. S4 and S6). However, distinguishing between molecules with exactly the same mass and product ions, such as SM (d18:1/18:0) and SM (d20:1/16:0), was not possible. This effect is a limitation of MALDI-IMS. However, it has been described that d18:1 Sph is present in all sphingolipids, in contrast to d20:1 Sph, which is a constituent of only gangliosides [47]. Furthermore, we undertook structural analyses of SM (36:1), LacCer (36:1) and LacCer (38:1) by MS/MS using LC/ESI-MS/MS because C18:0 acyl-chain-containing SM and LacCer are major molecular species in the brain. As a result, we confirmed that only d18:1 Sph-containing SM was present, whereas d18:1 Sph- and d20:1 Sph-containing LacCers were present in the brain. Thus, our MALDI-IMS experiments enabled visualization of the expected d18:1 Sph-containing SM species.

We demonstrated that SM (d18:1/18:0) was distributed in the GM, whereas SM

(d18:1/24:1) was distributed in the WM in mouse brain sections using MALDI-TOF-IMS and ultra-high-resolution MALDI-FTICR-IMS. Delvolve et al. also revealed SM (d18:1/18:0) to be distributed in the GM, and SM (d18:1/24:1) to be distributed in the WM, in rat brain sections using MALDI-LTQ-XL [38]. Even though we used a different method and animal species, our results were in good agreement with their data. Thus, these results suggest that SM distribution is different and that its molecular functions may be regulated according to the lengths of acyl-chains in the brain. However, the relationship between the molecular species of SM and their regulatory synthases is incompletely understood.

Different profiles of SM and Cer among tissues such as brain, liver and kidneys have been previously described [23, 28]. For example, C24 VLCFAs are major components of SM and Cer in the liver and kidneys, whereas C18 LCFAs are major components of SM and Cer in the brain and skeletal muscle [23, 48]. Besides, it has also been reported that acyl-CoA compositions do not correlate with the respective Cer compositions among tissues [48]. These reports suggest that their profiles are determined by the expression pattern of their synthases, while acyl-CoA availability seems to be less important. SMS is responsible for SM synthesis [16, 17, 20], but SMS has no specificity for the different lengths of acyl-chains of Cer. In contrast to SMS, CerS exhibits restricted substrate specificity to FAs with specific chain lengths and ubiquitous or tissue-specific distribution patterns [21–23, 48]. CerS1 (which is responsible for the synthesis of C18 LCFA-containing sphingolipids) is specifically expressed in the brain and skeletal muscle, while CerS2 (which is responsible for the synthesis of C22–C24 VLCFA-containing

sphingolipids) is expressed widely in all organs [48]. We also evaluated the expression of the CerS family in the forebrain and cerebellum to ascertain the relationship between the profiles of SM and CerS in these tissues. Similar to previous reports [48], CerS1 and CerS2 were expressed in these organs, as well as SM (d18:1/18:0), Cer (d18:1/18:0), SM (d18:1/24:1) and SM (d18:1/24:1). Although other enzymes involved in sphingolipid synthesis also influence the compositions of SM with distinct lengths of acyl-chains in each cell type, these results suggest that expression patterns of CerS family members is correlated with a SM profile that is similar to Cer, at least in the brain. Therefore, we speculate that expression of CerS family members determines the spatial distributions of SM molecular species according to their substrate specificity in the reaction steps of Cer synthesis.

We also compared the expressions of CerS1 and CerS2 with the distributions of SM (d18:1/18:0) and SM (d18:1/24:1) in brain sections using ISH and MALDI-FTICR-IMS to identify their relationship within the brain. CerS2 expression was detected strongly in the WM, including the WM of the cerebellum, Tha, CC, Fi, AC and OT, as described previously [25, 26, 28, 49]. VLCFA-containing SMs, such as SM (d18:1/24:1), were also localized specifically in the myelin-rich WM, similar to CerS2. These results suggest that CerS2 mainly regulates production of VLCFA-containing SMs in oligodendrocytes. In contrast, SM (d18:1/18:0) was distributed widely in the GM of Hip, Hy, AO, VS, SN, CPu and Cx in the brain. CerS1 was also expressed widely in the GM, as described previously [24, 25]. These observations suggest that CerS1 mainly regulates production of SM

(d18:1/18:0) in neuronal cells. We could not visualize Cer distribution because of its low concentration and poor ionization. However, Roux et al. demonstrated Cer (d18:1/18:0) to be distributed in the GM, whereas Cer (d18:1/24:1) as well as SM have been shown to be distributed in the WM in mouse brain sections using silver nanoparticles and MALDI-LTQ-Orbitrap [50]. Additionally, we evaluated the contribution of CerS2 on the composition of SM by siRNA treatment in HepG2 cells. CerS2 suppression specifically decreased C22 VLCFA- and C24 VLCFA-containing SMs, whereas SMS2 suppression widely decreased the number of SM species. These results suggested that the composition and distribution of SM could be determined at least in part by the expression pattern of CerS isoforms.

To clarify the relationship between the lengths of acyl-chains of SM and CerS, evaluation of the distribution of glycosphingolipids (GSLs) is important because GSLs are also produced from Cer and major metabolites of Cer as well as SM in the brain. Cer can be converted to galactosylceramide (GalCer) by UDP-galactose ceramide galactosyltransferase (Cgt) in the ER of the brain to maintain the functions and structures of myelin, whereas most Cer molecules are converted to GlcCer by Ugcg and then to more complex gangliosides such as GM3 in the Golgi after transportation from the ER [18]. It has been revealed that GalCer is a major HexCer in the brain, whereas GlcCer is a major HexCer in the liver and kidneys [28, 46]. It has also been reported that GlcCer (and subsequently LacCer and gangliosides) contain mainly C18 LCFA, whereas GalCer (and subsequently sulfatides) contain mainly C22–C24 VLCFAs in the brain [51]. We revealed

HexCer (d18:1/24:1) to also be localized in the WM of the brain, similarly to SM (d18:1/24:0) and SM (d18:1/24:1). Goto-Inoue et al. also reported localization of GSLs, including sulfatides and gangliosides, in mouse brains using gold nanoparticles and MALDI-TOF-IMS [52]. In their reports, sulfatides (d18:1/24:1) were localized in the WM, whereas GM3 (d18:1/18:0), GM2 (d18:1/18:0), GM1 (d18:1/18:0), and GD1 (d18:1/18:0) were in the GM. Furthermore, it has been reported that Ugcg is highly expressed in C18 LCFA-containing LacCer and ganglioside-rich GM in the brain [53]. In contrast, it has also been reported that Cgt is highly expressed in C22 VLCFA- or C24 VLCFA-containing GalCer and sulfatide-rich WM in the brain [54]. These reports suggest that expression of the synthases of GSLs and distribution of GSLs are also similar to Cer species in terms of lengths of acyl-chains. These reports strongly support the notion that the distribution of sphingolipid molecular species, including SM and GSL, is dependent on the localization of CerS isoforms and subsequent Cer molecular species. The importance of such variety is incompletely understood, but C24 VLCFA-containing sphingolipids are localized in Schwann cells and myelin-rich WM. Ginkel et al. found that CerS1 deficiency causes reductions in levels of C18 LCFA-containing Cer, SM and gangliosides and expression of oligodendrocytic myelin-associated glycoprotein in mice [24]. It has also been demonstrated that CerS2 deficiency results in reductions of levels of C24 VLCFA-containing Cer, SM and GalCer as well as myelin-sheath defects in mouse brains [28, 49]. Therefore, these results strongly suggest that the molecular function of SM is dependent on the lengths of acyl-chains and regulated by the distribution of Cer, and that VLCFA-containing sphingolipids might be important molecules in maintenance of the

structure of myelin sheaths.

## **5. Conclusion**

Our study is the first comparison of SM molecular species and CerS distribution using molecular imaging, and revealed that different tissue distributions of SM species are associated with the expression of particular CerS in the brain. Thus, histological analyses of SM species by IMS could be a useful approach to consider their molecular function and mechanism of regulation upon combination with other imaging techniques.

### **Conflict of interest**

The authors declare that there is no conflict of interest associated with this manuscript.

### **Author contributions**

- M.S. undertook the acquisition and analysis (animal experiments, lipid measurements, lipid imaging, quantitative real-time PCR) of data, designed the study, drafted the manuscript and created the figures.
- M.W. assembled the apparatus for the extraction and measurement of lipids.
- Y.T. set the MALDI-TOF-MS condition for SM imaging.
- Y.S., T.Y., K.H., Y.N., S.S., A.K. and Y.I. participated in the study conception and advised on the study concept.
- Y.K. was responsible for the study conception and drafted the manuscript.
- All authors contributed to editing the final version of the manuscript.

### **Acknowledgements**

This study was supported by the Creation of Innovation Centers for Advanced Interdisciplinary Research Areas Program, Ministry of Education, Culture, Sports, Science and Technology, Japan, and a grant from Shionogi & Co., Ltd. We thank Yoko Ebita, Reimi Kishi and Bruker Daltonics for their skillful technical assistance.

## References

- [1] D. Milhas, C.J. Clarke, Y.A. Hannun, Sphingomyelin metabolism at the plasma membrane: implications for bioactive sphingolipids, *FEBS Lett.* 584 (2010) 1887–1894.
- [2] K. Simons, M.J. Gerl, Revitalizing membrane rafts: new tools and insights, *Nat. Rev. Mol. Cell. Biol.* 11 (2010) 688–699.
- [3] D. Lingwood, K. Simons, Lipid rafts as a membrane-organizing principle, *Science.* 327 (2010) 46–50.
- [4] T. Wennekes, R.J. van den Berg, R.G. Boot, G.A. van der Marel, H.S. Overkleeft, J.M. Aerts, Glycosphingolipids – nature, function, and pharmacological modulation, *Angew Chem. Int. Ed. Engl.* 48 (2009) 8848–8869.
- [5] M. Miyaji, Z.X. Jin, S. Yamaoka, R. Amakawa, S. Fukuhara, S.B. Sato, T. Kobayashi, N. Domae, T. Mimori, E.T. Bloom, T. Okazaki and H. Umehara, Role of membrane sphingomyelin and ceramide in platform formation for Fas-mediated apoptosis, *J. Exp. Med.* 202 (2005) 249–259.
- [6] N.D. Ridgway, Interactions between metabolism and intracellular distribution of cholesterol and sphingomyelin, *Biochim. Biophys. Acta.* 1484 (2000) 129–141.
- [7] S. Asano, K. Kitatani, M. Taniguchi, M. Hashimoto, K. Zama, S. Mitsutake, Y. Igarashi, H. Takeya, J. Kigawa, A. Hayashi, H. Umehara, T. Okazaki, Regulation of cell migration by sphingomyelin synthases: sphingomyelin in lipid rafts decreases responsiveness to signaling by the CXCL12/CXCR4 pathway, *Mol. Cell. Biol.* 32 (2012) 3242–3252.

- [8] S. Mitsutake, K. Zama, H. Yokota, T. Yoshida, M. Tanaka, M. Mitsui, M. Ikawa, M. Okabe, Y. Tanaka, T. Yamashita, H. Takemoto, T. Okazaki, K. Watanabe, Y. Igarashi, Dynamic modification of sphingomyelin in lipid microdomains controls development of obesity, fatty liver, and type 2 diabetes, *J. Biol. Chem.* 286 (2011) 28544–28555.
- [9] Z. Li, H. Zhang, J. Liu, C.P. Liang, Y. Li, Y. Li, G. Teitelman, T. Beyer, H.H. Bui, D.A. Peake, Y. Zhang, P.E. Sanders, M.S. Kuo, T.S. Park, G. Cao, X.C. Jiang, Reducing plasma membrane sphingomyelin increases insulin sensitivity, *Mol. Cell. Biol.* 31 (2011) 4205–4218.
- [10] Y. Li, J. Dong, T. Ding, M.S. Kuo, G. Cao, X.C. Jiang, Z. Li, Sphingomyelin synthase 2 activity and liver steatosis: an effect of ceramide-mediated peroxisome proliferator-activated receptor  $\gamma$ 2 suppression, *Arterioscler. Thromb. Vasc. Biol.* 33 (2013), 1513–1520.
- [11] M.M. Hussain, W. Jin, X.C. Jiang, Mechanisms involved in cellular ceramide homeostasis, *Nutr. Metab. (Lond.)* 9 (2012) 71.
- [12] A.H. Merrill, Jr., Characterization of serine palmitoyltransferase activity in Chinese hamster ovary cells, *Biochim. Biophys. Acta.* 754 (1983) 284–291.
- [13] D.S. Menaldino, A. Bushnev, A. Sun, D.C. Liotta, H. Symolon, K. Desai, D.L. Dillehay, Q. Peng, E. Wang, J. Allegood, S. Trotman-Pruett, M.C. Sullards, A.H. Merrill, Jr., Sphingoid bases and *de novo* ceramide synthesis: enzymes involved, pharmacology and mechanisms of action, *Pharmacol. Res.* 47 (2003) 373–381.
- [14] K. Hanada, K. Kumagai, S. Yasuda, Y. Miura, M. Kawano, M. Fukasawa, M.

- Nishijima, Molecular machinery for non-vesicular trafficking of ceramide, *Nature*. 426 (2003) 803–809.
- [15] K. Hanada, K. Kumagai, N. Tomishige, T. Yamaji, CERT-mediated trafficking of ceramide, *Biochim. Biophys. Acta*. 1791 (2009) 684–691.
- [16] K. Huitema, J. van den Dikkenberg, J.F. Brouwers, J. C. Holthuis, Identification of a family of animal sphingomyelin synthases, *EMBO. J.* 23 (2004) 33–44.
- [17] S. Yamaoka, M. Miyaji, T. Kitano, H. Umehara, T. Okazaki, Expression cloning of a human cDNA restoring sphingomyelin synthesis and cell growth in sphingomyelin synthase-defective lymphoid cells, *J. Biol. Chem.* 279 (2004) 18688–18693.
- [18] S. Degroote, J. Wolthoorn, G. van Meer, The cell biology of glycosphingolipids, *Semin. Cell. Dev. Biol.* 15 (2004) 375–387.
- [19] R. Jennemann, R. Sandhoff, S. Wang, E. Kiss, N. Gretz, C. Zuliani, A. Martin-Villalba, R. Jager, H. Schorle, M. Kenzelmann, M. Bonrouhi, H. Wiegandt, H.J. Grone, Cell-specific deletion of glucosylceramide synthase in brain leads to severe neural defects after birth, *Proc. Natl. Acad. Sci. U. S. A.* 102 (2005) 12459–12464.
- [20] M. Taniguchi, T. Okazaki, The role of sphingomyelin and sphingomyelin synthases in cell death, proliferation and migration-from cell and animal models to human disorders, *Biochim. Biophys. Acta*. 1841 (2014) 692–703.
- [21] Y. Mizutani, S. Mitsutake, K. Tsuji, A. Kihara, Y. Igarashi, Ceramide biosynthesis in keratinocyte and its role in skin function, *Biochimie*. 91 (2009) 784–790.
- [22] M. Levy, A.H. Futerman, Mammalian ceramide synthases, *IUBMB. Life*. 62 (2010)

347–356.

- [23] T. Sassa, A. Kihara, Metabolism of very long-chain fatty acids: genes and pathophysiology, *Biomol. Ther. (Seoul)* 22 (2014) 83–92.
- [24] C. Ginkel, D. Hartmann, K. vom Dorp, A. Zlomuzica, H. Farwanah, M. Eckhardt, R. Sandhoff, J. Degen, M. Rabionet, E. Dere, P. Dormann, K. Sandhoff, K. Willecke, Ablation of neuronal ceramide synthase 1 in mice decreases ganglioside levels and expression of myelin-associated glycoprotein in oligodendrocytes, *J. Biol. Chem.* 287 (2012) 41888–41902.
- [25] I. Becker, L. Wang-Eckhardt, A. Yaghootfam, V. Gieselmann, M. Eckhardt, Differential expression of (dihydro)ceramide synthases in mouse brain: oligodendrocyte-specific expression of CerS2/Lass2, *Histochem. Cell. Biol.* 129 (2008) 233–241.
- [26] C. Kremser, A.L. Klemm, M. van Uelft, S. Imgrund, C. Ginkel, D. Hartmann, K. Willecke, Cell-type-specific expression pattern of ceramide synthase 2 protein in mouse tissues, *Histochem. Cell. Biol.* 140 (2013) 533–547.
- [27] Y. Pewzner-Jung, H. Park, E.L. Laviad, L.C. Silva, S. Lahiri, J. Stiban, R. Erez-Roman, B. Brugger, T. Sachsenheimer, F. Wieland, M. Prieto, A.H. Merrill, Jr., A.H. Futerman, A critical role for ceramide synthase 2 in liver homeostasis: I. alterations in lipid metabolic pathways, *J. Biol. Chem.* 285 (2010) 10902–10910.
- [28] S. Imgrund, D. Hartmann, H. Farwanah, M. Eckhardt, R. Sandhoff, J. Degen, V. Gieselmann, K. Sandhoff, K. Willecke, Adult ceramide synthase 2 (CERS2)-deficient mice exhibit myelin sheath defects, cerebellar degeneration, and

- hepatocarcinomas, *J. Biol. Chem.* 284 (2009) 33549–33560.
- [29] M. Stoeckli, P. Chaurand, D.E. Hallahan, R.M. Caprioli, Imaging mass spectrometry: a new technology for the analysis of protein expression in mammalian tissues, *Nat. Med.* 7 (2001) 493–496.
- [30] P.J. Todd, T.G. Schaaff, P. Chaurand, R.M. Caprioli, Organic ion imaging of biological tissue with secondary ion mass spectrometry and matrix-assisted laser desorption/ionization, *J. Mass. Spectrom.* 36 (2001) 355–369.
- [31] M. Irie, Y. Fujimura, M. Yamato, D. Miura, H. Wariishi, Integrated MALDI-MS imaging and LC-MS techniques for visualizing spatiotemporal metabolomic dynamics in a rat stroke model, *Metabolomics.* 10 (2014) 473–483.
- [32] N. Takai, Y. Tanaka, H. Saji, Quantification of small molecule drugs in biological tissue sections by imaging mass spectrometry using surrogate tissue-based calibration standards, *Mass. Spectrom. (Tokyo)* 3 (2014) A0025.
- [33] N. Takai, Y. Tanaka, K. Inazawa, H. Saji, Quantitative analysis of pharmaceutical drug distribution in multiple organs by imaging mass spectrometry, *Rapid. Commun. Mass. Spectrom.* 26 (2012) 1549–1556.
- [34] E.E. Jones, S. Dworski, D. Canals, J. Casas, G. Fabrias, D. Schoenling, T. Levade, C. Denlinger, Y.A. Hannun, J.A. Medin, R.R. Drake, On-tissue localization of ceramides and other sphingolipids by MALDI mass spectrometry imaging, *Anal. Chem.* 86 (2014) 8303–8311.
- [35] Y. Sugiura, Y. Konishi, N. Zaima, S. Kajihara, H. Nakanishi, R. Taguchi, M. Setou, Visualization of the cell-selective distribution of PUFA-containing

- phosphatidylcholines in mouse brain by imaging mass spectrometry, *J. Lipid Res.* 50 (2009) 1776–1788.
- [36] K. Shrivastava, T. Hayasaka, N. Goto-Inoue, Y. Sugiura, N. Zaima, M. Setou, Ionic matrix for enhanced MALDI imaging mass spectrometry for identification of phospholipids in mouse liver and cerebellum tissue sections, *Anal. Chem.* 82 (2010) 8800–8806.
- [37] H. Enomoto, Y. Sugiura, M. Setou, N. Zaima, Visualization of phosphatidylcholine, lysophosphatidylcholine and sphingomyelin in mouse tongue body by matrix-assisted laser desorption/ionization imaging mass spectrometry, *Anal. Bioanal. Chem.* 400 (2011) 1913–1921.
- [38] A.M. Delvolve, B. Colsch, A.S. Woods, Highlighting anatomical sub-structures in rat brain tissue using lipid imaging, *Anal. Methods.* 3 (2011) 1729–1736.
- [39] T. Hayasaka, N. Goto-Inoue, Y. Sugiura, N. Zaima, H. Nakanishi, K. Ohishi, S. Nakanishi, T. Naito, R. Taguchi, M. Setou, Matrix-assisted laser desorption/ionization quadrupole ion trap time-of-flight (MALDI-QIT-TOF)-based imaging mass spectrometry reveals a layered distribution of phospholipid molecular species in the mouse retina, *Rapid. Commun. Mass. Spectrom.* 22 (2008) 3415–3426.
- [40] S. Shimma, Y. Sugiura, T. Hayasaka, N. Zaima, M. Matsumoto, M. Setou, Mass imaging and identification of biomolecules with MALDI-QIT-TOF-based system, *Anal. Chem.* 80 (2008) 878–885.
- [41] Y. Fujimura, D. Miura, MALDI mass spectrometry imaging for visualizing *in situ*

- metabolism of endogenous metabolites and dietary phytochemicals, *Metabolites*. 4 (2014) 319–346.
- [42] D. Miura, Y. Tsuji, K. Takahashi, H. Wariishi, K. Saito, A strategy for the determination of the elemental composition by Fourier transform ion cyclotron resonance mass spectrometry based on isotopic peak ratios, *Anal. Chem.* 82 (2010) 5887–5891.
- [43] D.S. Cornett, S.L. Frappier, R.M. Caprioli, MALDI-FTICR imaging mass spectrometry of drugs and metabolites in tissue, *Anal. Chem.* 80 (2008) 5648–5653.
- [44] E.G. Bligh, W.J. Dyer, A rapid method of total lipid extraction and purification, *Can. J. Biochem. Physiol.* 37 (1959) 911–917.
- [45] P.I. Castagnet, M.Y. Golovko, G.C. Barceló-Coblijn, R.L. Nussbaum, E.J. Murphy, Fatty acid incorporation is decreased in astrocytes cultured from alpha-synuclein gene-ablated mice, *J. Neurochem.* 94 (2005) 839–849.
- [46] T. Yamada, T. Uchikata, S. Sakamoto, Y. Yokoi, E. Fukusaki, T. Bamba, Development of a lipid profiling system using reverse-phase liquid chromatography coupled to high-resolution mass spectrometry with rapid polarity switching and an automated lipid identification software, *J. Chromatogr. A*. 1292 (2013) 211–218.
- [47] B. Colsch, C. Afonso, I. Popa, J. Portoukalian, F. Fournier, J.C. Tabet, N. Baumann, Characterization of the ceramide moieties of sphingoglycolipids from mouse brain by ESI-MS/MS: identification of ceramides containing sphingadienine, *J. Lipid Res.* 45 (2004) 281–286.
- [48] S. Schiffmann, K. Birod, J. Mannich, M. Eberle, M.S. Wegner, R. Wanger, D.

- Hartmann, N. Ferreiros, G. Geisslinger, S. Grosch, Ceramide metabolism in mouse tissue, *Int. J. Biochem. Cell. Biol.* 45 (2013) 1886–1894.
- [49] O. Ben-David, Y. Pewzner-Jung, O. Brenner, E.L. Laviad, A. Kogot-Levin, I. Weissberg, I.E. Biton, R. Pienik, E. Wang, S. Kelly, J. Alroy, A. Raas-Rothschild, A. Friedman, B. Brugger, A.H. Merrill, Jr., A.H. Futerman, Encephalopathy caused by ablation of very long acyl chain ceramide synthesis may be largely due to reduced galactosylceramide levels, *J. Biol. Chem.* 286 (2011) 30022–30033.
- [50] A. Roux, L. Muller, S.N. Jackson, K. Baldwin, V. Womack, J.G. Pagiazitis, J.R. O'Rourke, P.K. Thanos, C. Balaban, J.A. Schultz, N.D. Volkow, A.S. Woods, Chronic ethanol consumption profoundly alters regional brain ceramide and sphingomyelin content in rodents, *ACS. Chem. Neurosci.* 18 (2015) 247–259.
- [51] K. Ikeda, R. Taguchi, Highly sensitive localization analysis of gangliosides and sulfatides including structural isomers in mouse cerebellum sections by combination of laser microdissection and hydrophilic interaction liquid chromatography/electrospray ionization mass spectrometry with theoretically expanded multiple reaction monitoring, *Rapid Commun. Mass Spectrom.* 24 (2010) 2957–2965.
- [52] N. Goto-Inoue, T. Hayasaka, N. Zaima, Y. Kashiwagi, M. Yamamoto, M. Nakamoto, M. Setou, The detection of glycosphingolipids in brain tissue sections by imaging mass spectrometry using gold nanoparticles, *J. Am. Soc. Mass. Spectrom.* 21 (2010) 1940–1943.
- [53] V. Nordström, M. Willershäuser, S. Herzer, J. Rozman, O. von Bohlen Und Halbach,

S. Meldner, U. Rothermel, S. Kaden, F.C. Roth, C. Waldeck, N. Gretz, M.H. de Angelis, A. Draguhn, M. Klingenspor, HJ. Gröne, R. Jennemann, Neuronal expression of glucosylceramide synthase in central nervous system regulates body weight and energy homeostasis, *PLoS Biol.* 11 (2013) e1001506.

- [54] S.N. Fewou, H. Büssow, N. Schaeren-Wiemers, M.T. Vanier, W.B. Macklin, V. Gieselmann, M. Eckhardt, Reversal of non-hydroxy:alpha-hydroxy galactosylceramide ratio and unstable myelin in transgenic mice overexpressing UDP-galactose:ceramide galactosyltransferase, *J. Neurochem.* 94 (2005) 469–481.

### Figure legends

Figure 1. Composition of SM and Cer, and expression of CerS family members in mouse brain. Individual acyl-chains of SM in forebrain (A), cerebellum (B), Cer in forebrain (C) and cerebellum (D), and expression of individual CerS family members in the forebrain (E) and cerebellum (F) are shown. To enable better comparison, relative values for each SM and Cer species are shown with those of total SM and Cer normalized to 100% in A–D, and relative values for expression of CerS1 in the forebrain in E and F are shown. The x-axis indicates the lengths of acyl-chain of SM and Cer, and the y-axis indicates the SM and Cer compositions in A–D. The x-axis indicates the CerS isoforms and the y-axis indicates the relative expression of mRNA in E and F. Data are the mean  $\pm$  SD (n=3).

Figure 2. Representative spectra of SM and HexCer obtained from forebrain sections by MALDI-FTICR-IMS. H&E staining of forebrain (A). Obtained spectra at  $m/z$  740–744 (B), 765–772 (C), 824–828 (D) and 848–856 (E) from the lateral ventricle (LV), hippocampus (Hip) and corpus callosum (CC) in the forebrain. The x-axis indicates  $m/z$  and the y-axis indicates the signal intensity. Scale bar = 1 mm. These results were obtained from three individuals.

Figure 3. Representative images of SM molecular species in the forebrain. SM (d18:1/16:0) (A), SM (d18:1/18:0) (B), SM (d18:1/18:1) (C), SM (d18:1/22:0) (D), SM (d18:1/24:0) (E), SM (d18:1/24:1) (F), HexCer (d18:1/24:1) (G) and merged image of SM (d18:1/16:0), SM (d18:1/18:0) and SM (d18:1/24:1) (H) are shown. Scale bar = 1 mm. These results were

obtained from three individuals.

Figure 4. Representative spectra of SM and HexCer obtained from cerebellum sections by MALDI-FTICR-IMS. H&E staining of the cerebellum (A). Obtained spectra at  $m/z$  740–744 (B), 765–772 (C), 824–828 (D) and 848–856 (E) from the fourth ventricle (4V), molecular layer (ML) and white matter (WM) in the cerebellum. The x-axis indicates  $m/z$  and the y-axis indicates the signal intensity. Scale bar = 1 mm. These results were obtained from three individuals.

Figure 5. Representative images of SM molecular species in the cerebellum. SM (d18:1/16:0) (A), SM (d18:1/18:0) (B), SM (d18:1/18:1) (C), SM (d18:1/22:0) (D), SM (d18:1/24:0) (E), SM (d18:1/24:1) (F), HexCer (d18:1/24:1) (G) and merged image of SM (d18:1/16:0), SM (d18:1/18:0) and SM (d18:1/24:1) (H) are shown. Scale bar = 1 mm. These results were obtained from three individuals.

Figure 6. Representative tissue distribution of SM species and expression of CerS in mouse brain section. H&E staining (A) and KB staining (B and C) of brain sections. Cresyl-Violet-positive Nissl bodies (black arrows) and Luxol Fast-Blue-positive axons (white arrows) are shown. ISH of CerS1 (D) and CerS2 (E) are shown. IMS analysis of SM (d18:1/18:0) (F) and SM (d18:1/24:1) (G) are shown. Scale bars = 1 mm for A, B, D, E, F and G; and 200  $\mu$ m for C. These results were obtained from two individuals.

Figure 7. Responses of each SM molecular species to CerS2 and SMS2 suppression in HepG2 cells. Effects of CerS2 suppression on expression of CerS2 mRNA (A) and SM composition (B) by siRNAs for CerS2 treatment in HepG2 cells are shown. Effects of SMS2 suppression on expression of SMS2 mRNA (C) and SM composition (D) by siRNAs for SMS2 treatment in HepG2 cells are shown. The x-axis indicates the siRNA and the y-axis indicates the relative expression of mRNA in A and C. The x-axis indicates the SM molecular species and the y-axis indicates their concentrations in B and D. Data are the mean  $\pm$  SD (n=3). Experiments were repeated at least three times. Significant differences compared with negative control siRNA Number 1. \* $p$ <0.05, \*\* $p$ <0.01.

Figure 1

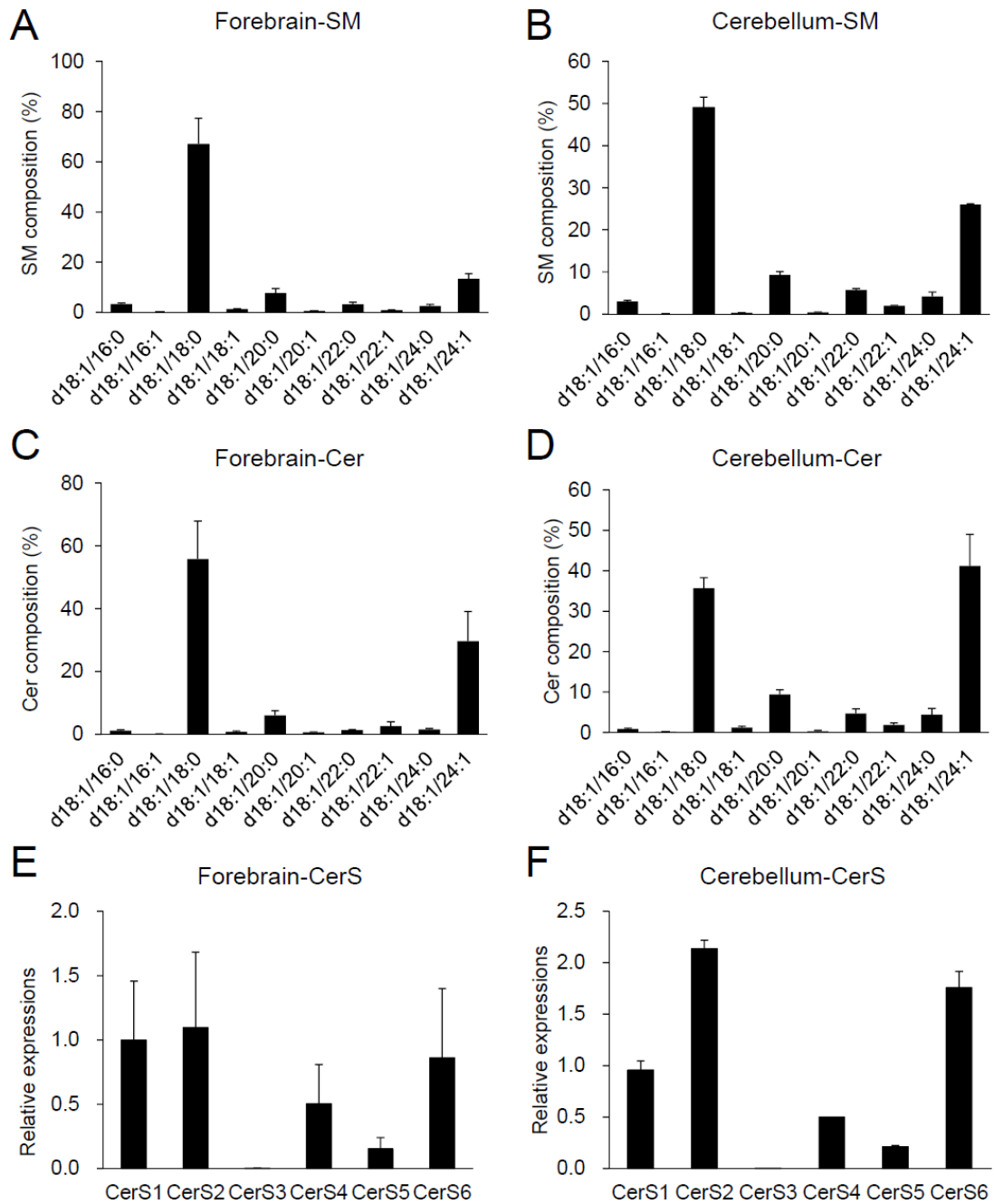
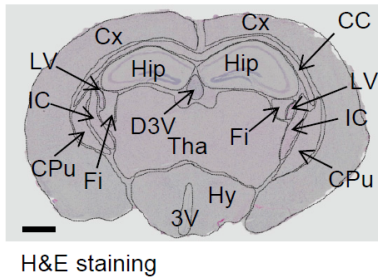
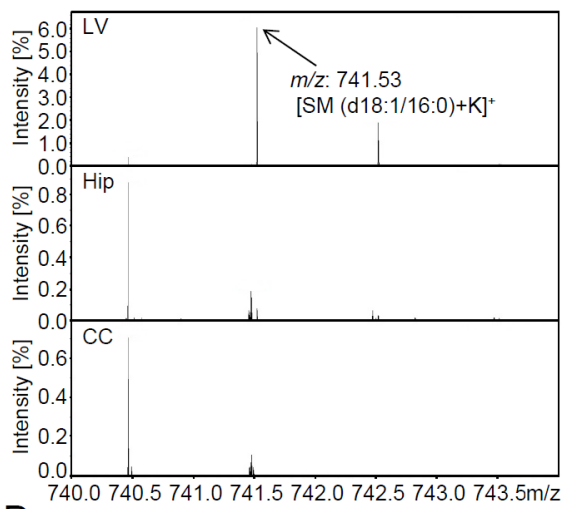


Figure 2

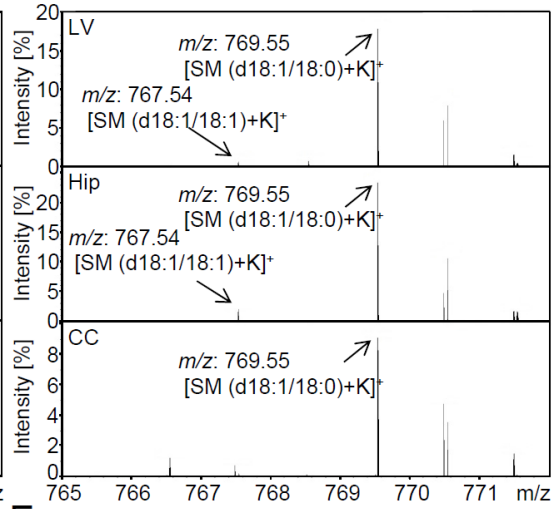
A



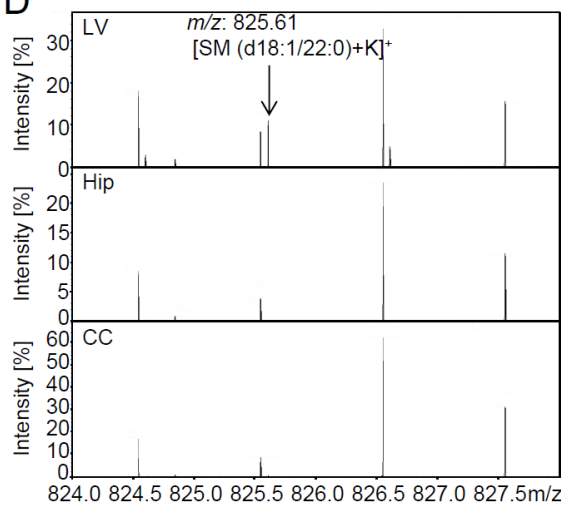
B



C



D



E

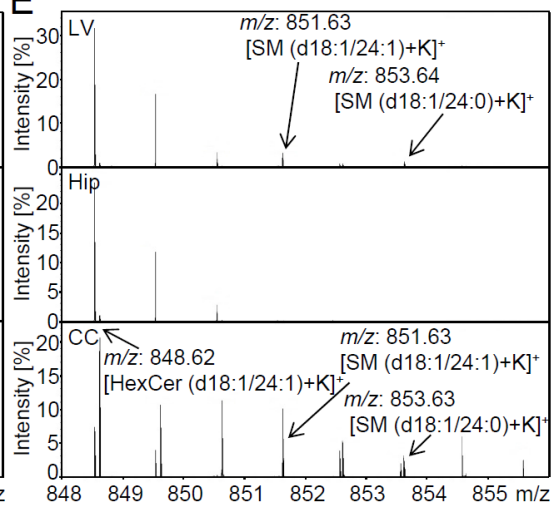


Figure 3

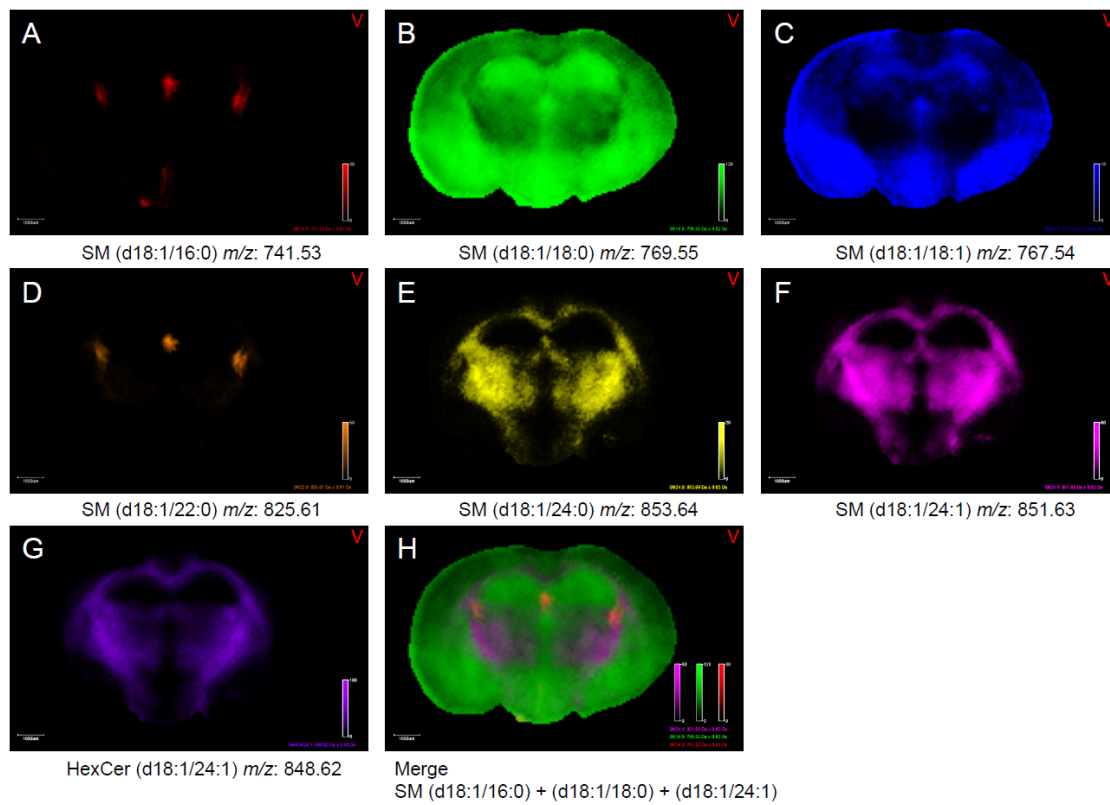
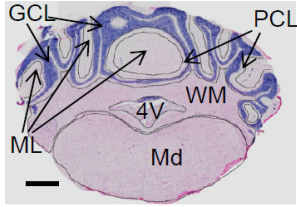


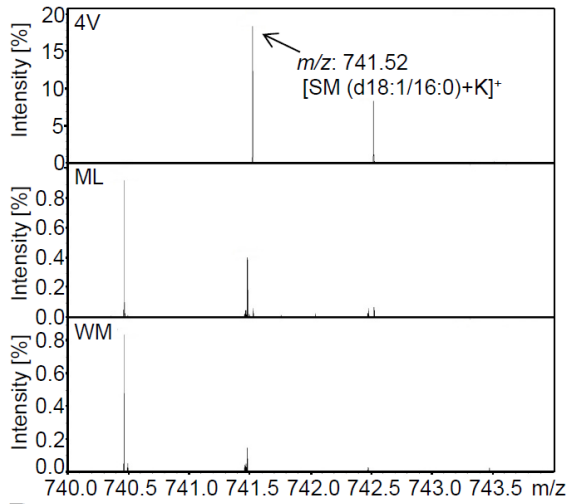
Figure 4

A

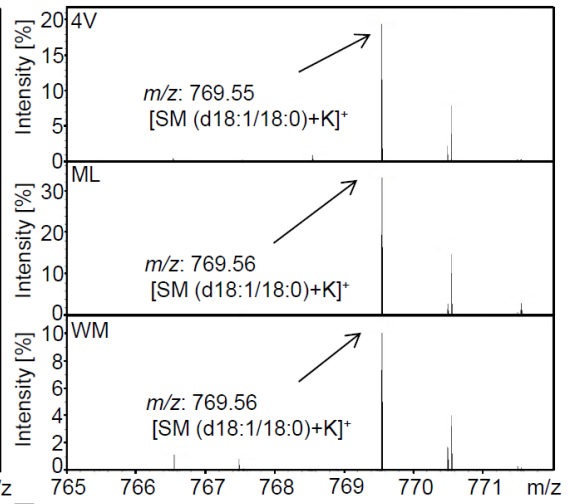


H&E staining

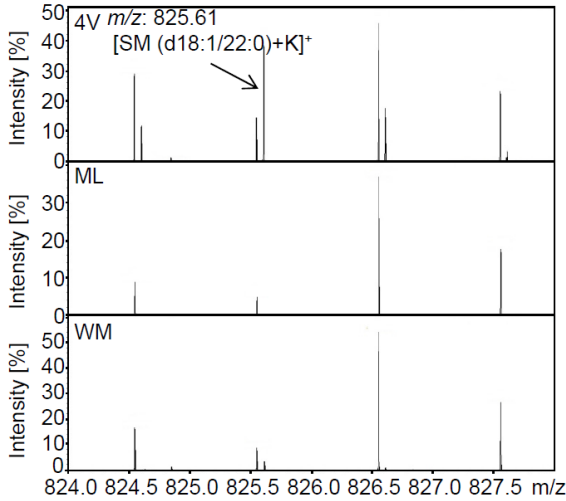
B



C



D



E

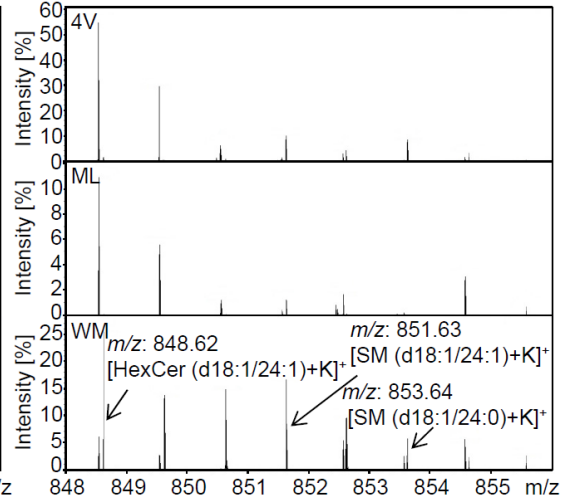
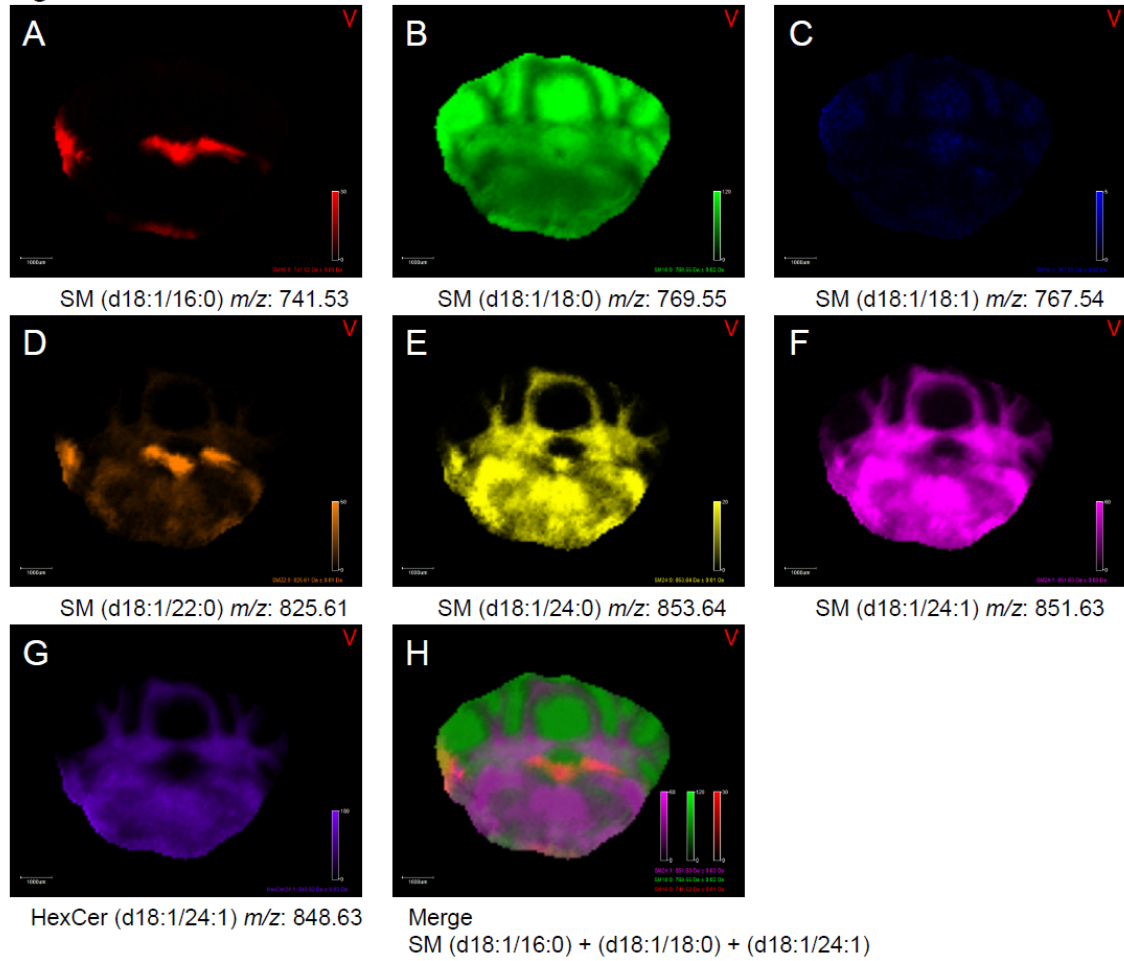
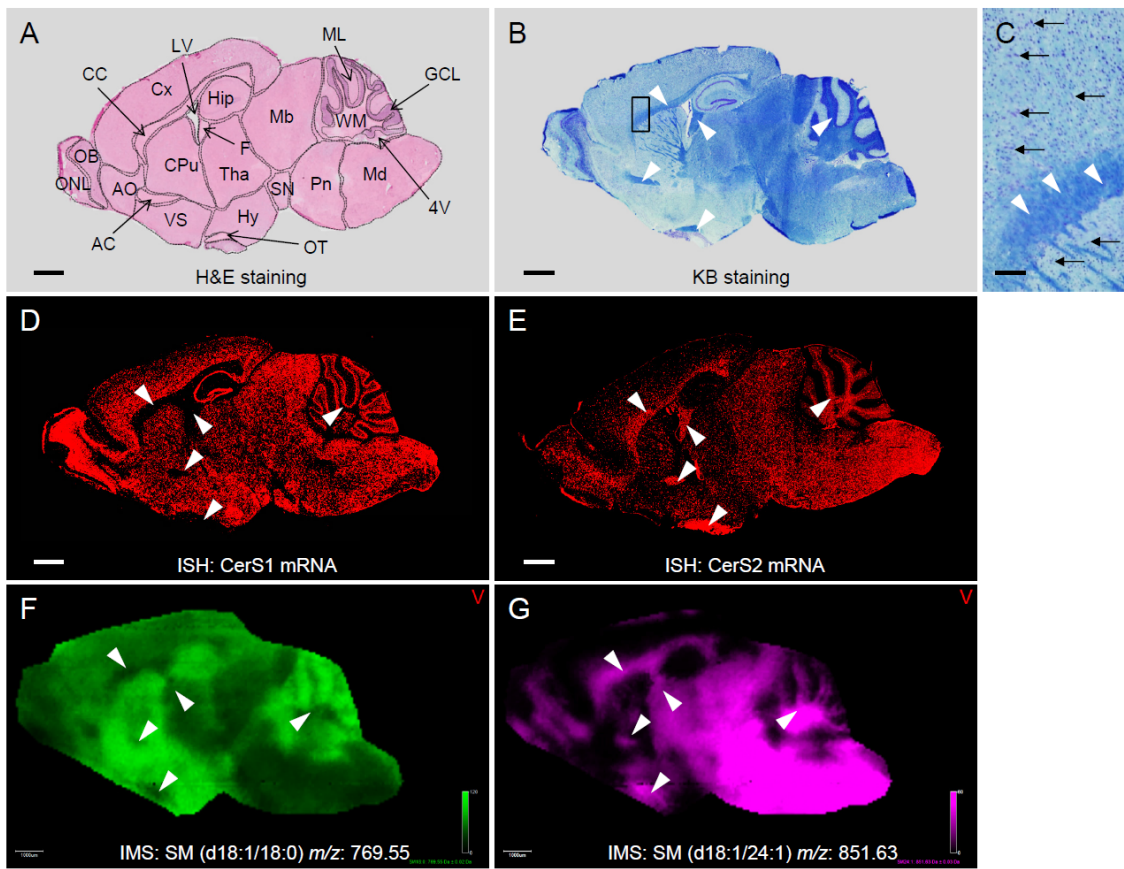
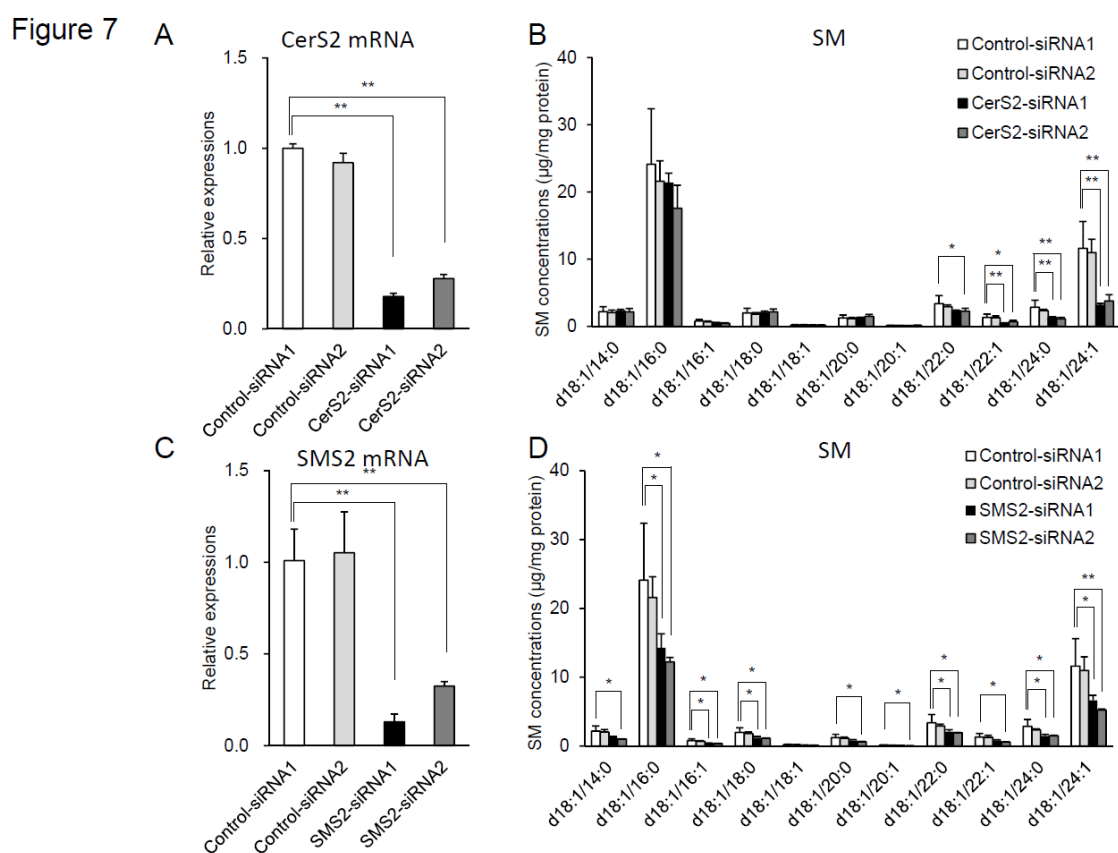


Figure 5







## Appendix A. Supplemental data

Supplemental Table 1. Summary of primer sets for quantitative real-time PCR.

Primers	Sequences 5'–3'
Mouse	
GAPDH Forward	TGTGTCCGTCGTGGATCTGA
GAPDH Reverse	TTGCTGTTGAAGTCGCAGGAG
CerS1 Forward	GGTCAGATGCGTGAAGTGGAA
CerS1 Reverse	GGATAGAGTCCTGGATGGCTGAA
CerS2 Forward	CGTGTCTATGCCAAAGCCTCA
CerS2 Reverse	GTCTGGTAGAAATGTTCCAAGGTG
CerS3 Forward	GCTGGATGGAAGCAGACGTGTA
CerS3 Reverse	TAGTGCAAAGGCAGGATCAGAGTG
CerS4 Forward	CATGACTGCTCCGACTACCTG
CerS4 Reverse	GAATATGAGGCGCGTGTAGAA
CerS5 Forward	ACGTGAGCGGCTCTGTACCA
CerS5 Reverse	GAGCACCTGCAGGATCAGGA

CerS6 Forward	CACCTGGGCAGACCTGAAGA
CerS6 Reverse	TGGCACATGGTTTGGCTATGA
Human	
RPS18 Forward	TTTGCGAGTACTCAACACCAACATC
RPS18 Reverse	GAGCATATCTTCGGCCACAC
CERS2 Forward	CATCCGAGCTGGGACTCTAATCA
CERS2 Reverse	GGGTACACCAGGGTGCAATG
SGMS2 Forward	ATTTCTGGTGGTGGATTGTCCATA
SGMS2 Reverse	CACTCAGCAGCCAGCAGATTA

Supplemental Figure 1. ISH of positive control and negative control in section of mouse brain. Representative ISH of glyceraldehyde 3-phosphate dehydrogenase (GAPDH) as positive control (A) and no probe as negative control (B) are shown. Scale bar = 1 mm. These results were obtained from two individuals.

Supplemental Figure 2. Structural analyses of LacCer (d18:1/18:0), LacCer (d20:1/18:0) and SM (d18:1/18:0) by LC/ESI-MS/MS. Obtained chromatogram (A), mass spectra of product ion at  $m/z$  70–790 (B), and 204–348 (C) from lipid extracts in the forebrain. The x-axis indicates the retention time and the y-axis indicates the signal intensity in A. The x-axis indicates  $m/z$  and the y-axis indicates the signal intensity in B and C.

Supplemental Figure 3. Spectra and isotopic compositions of SM and GalCer obtained from a sphingolipid standard mix by MALDI-FTICR-IMS. Obtained spectra at  $m/z$  740–745 (A), 766–772 (B), and 847–856 (C) from 50 ng of a spot of a sphingolipid standard mix. The x-axis indicates  $m/z$  and the y-axis indicates the signal intensity.

Supplemental Figure 4. Fragmentation of each SM standard on the ITO glass slide. Spectra of SM (d18:1/16:0), SM (d18:1/18:0), SM (d18:1/18:1), SM (d18:1/24:0) and SM (d18:1/24:1) were identified by on-tissue CID fragmentation at  $m/z$  741.50 (A), 769.55 (B), 767.51 (C), 853.60 (D) and 851.59 (E). The x-axis indicates  $m/z$  and the y-axis indicates the signal intensity.

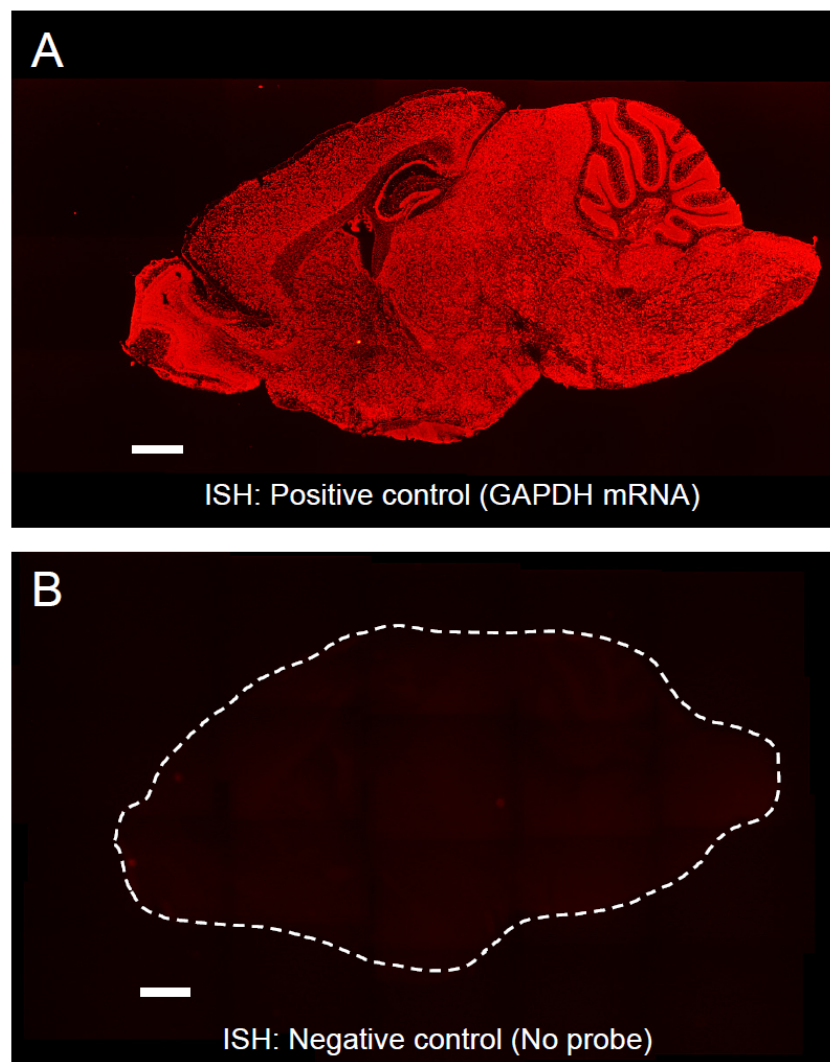
Supplemental Figure 5. Representative spectra and isotopic compositions of SM and HexCer obtained from forebrain sections by MALDI-FTICR-IMS. Obtained spectra at  $m/z$  740.5–744.5 (A), 766–772 (B), and 825–828 (C), 847–856 (D) from forebrain sections. Detailed spectra at  $m/z$  851.6 (D) and 853.6 (E). The x-axis indicates  $m/z$  and the y-axis indicates the signal intensity. These results were obtained from three individuals.

Supplemental Figure 6. On-tissue fragmentation of each SM molecular species in the forebrain. Spectra of SM (d18:1/16:0), SM (d18:1/18:0), SM (d18:1/24:0) and SM (d18:1/24:1) were identified by on-tissue CID fragmentation of  $m/z$  741.53 (A), 769.55 (B), 853.61 (C) and 851.64 (D). The x-axis indicates  $m/z$  and the y-axis indicates the signal intensity.

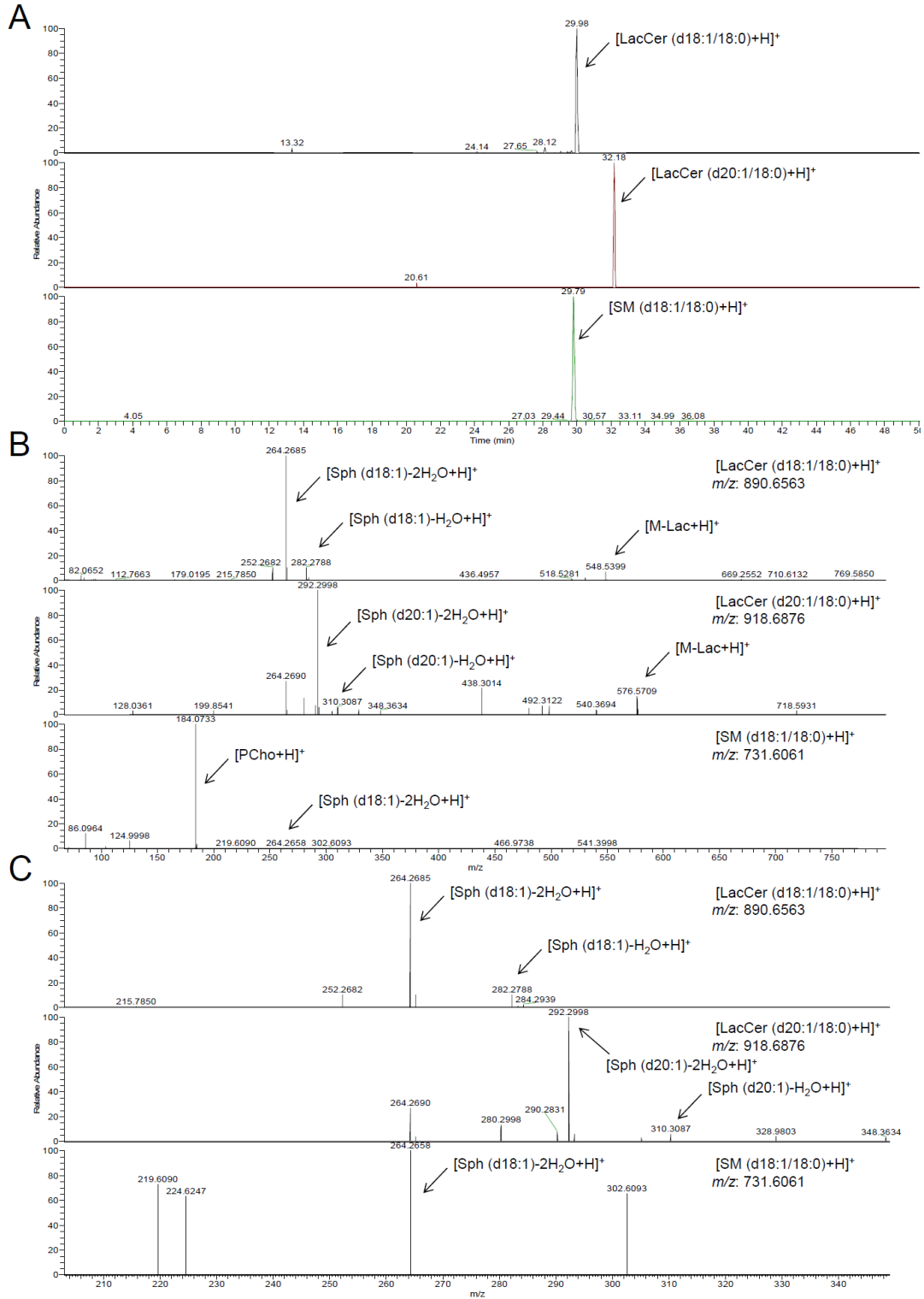
Supplemental Figure 7. Representative images of SM molecular species in the forebrain by MALDI-TOF-IMS. SM (d18:1/16:0) (A), SM (d18:1/18:0) (B), SM (d18:1/18:1) (C), SM (d18:1/22:0) (D), SM (d18:1/24:0) (E) and SM (d18:1/24:1) (F) are shown. These results were obtained from three individuals.

Supplemental Figure 8. Representative spectra of SM and HexCer obtained from forebrain sections by MALDI-TOF-IMS. Obtained spectra at  $m/z$  740–745 (A), 767–772 (B), and 823–828 (C), 848–855 (D) from forebrain sections. The x-axis indicates  $m/z$  and the y-axis indicates the signal intensity. These results were obtained from three individuals.

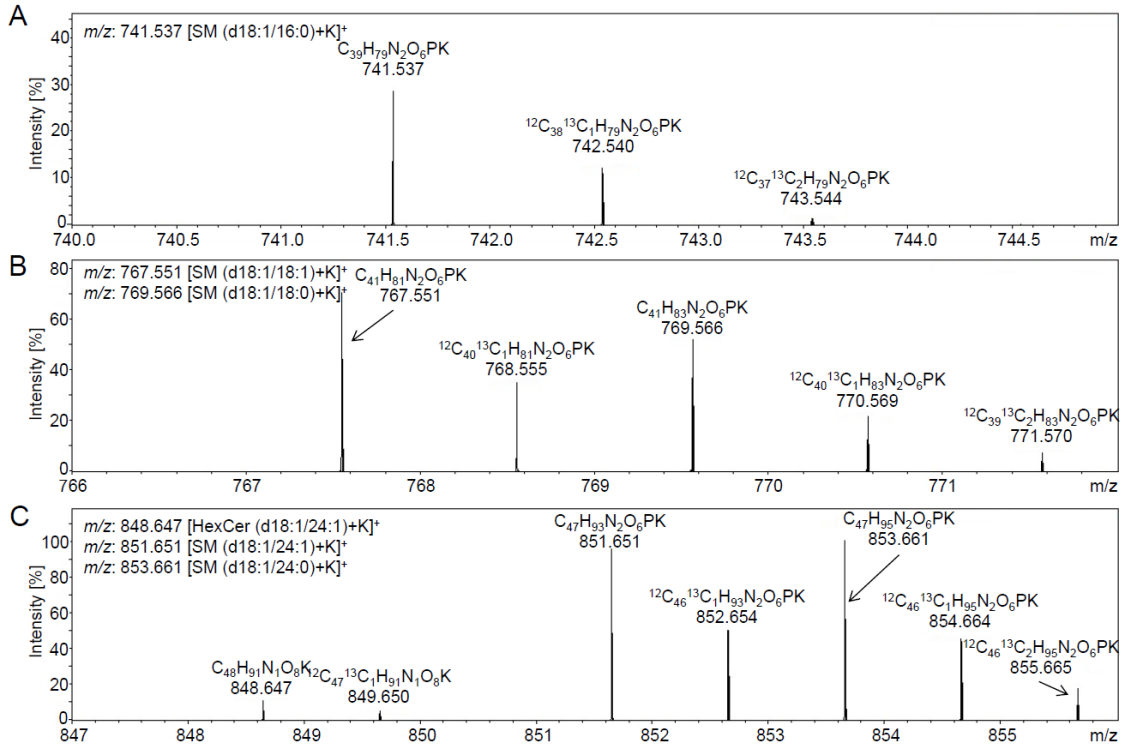
## Supplemental Figure 1



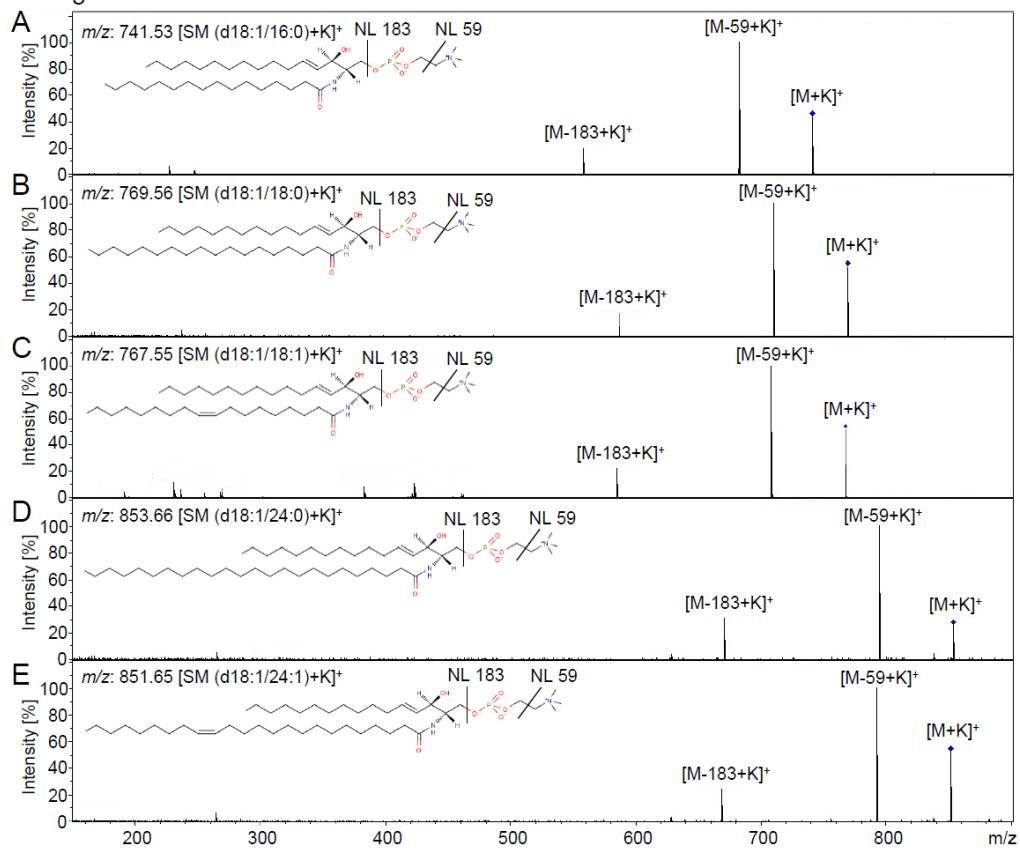
# Supplemental Figure 2



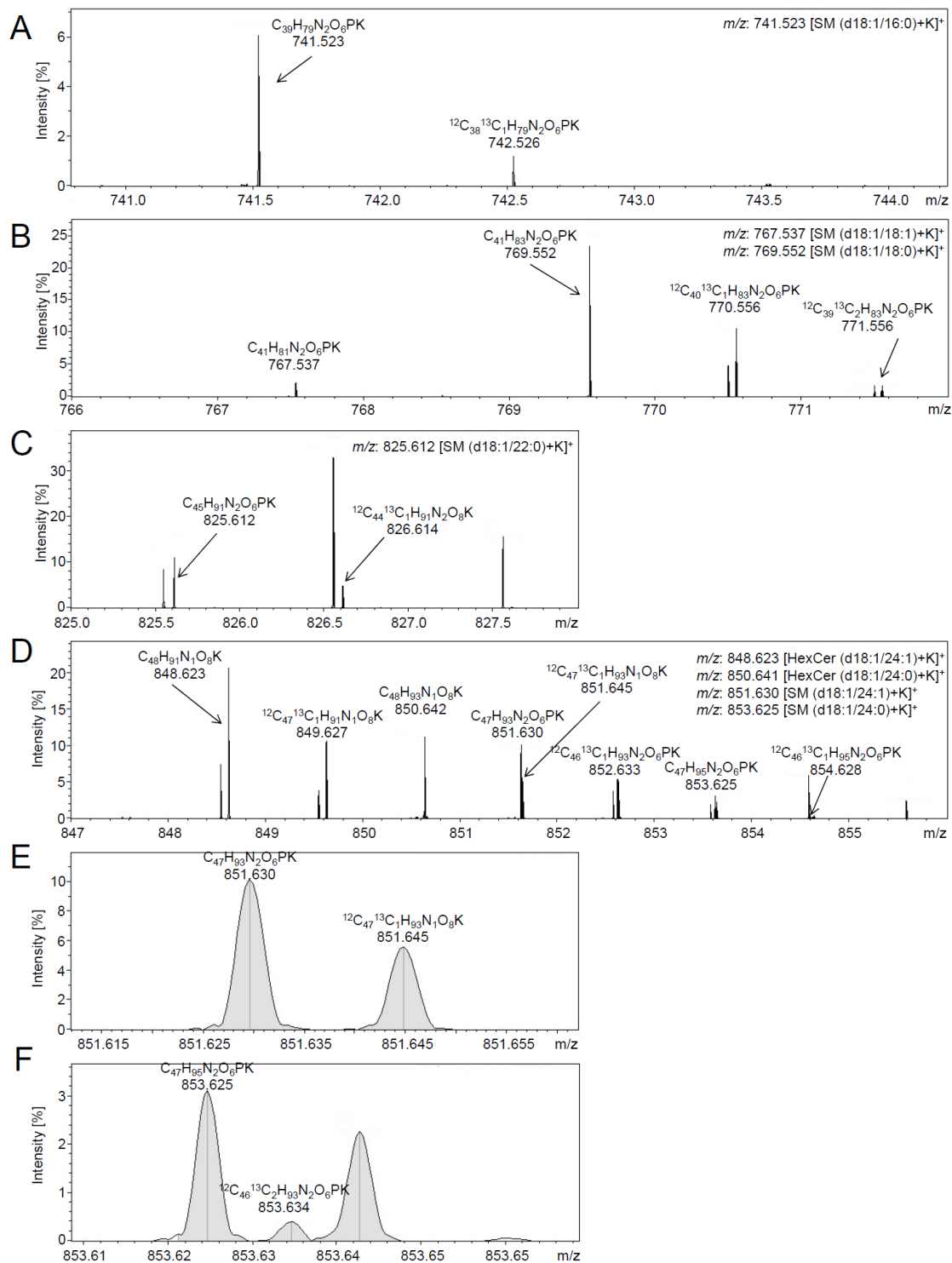
Supplemental Figure 3



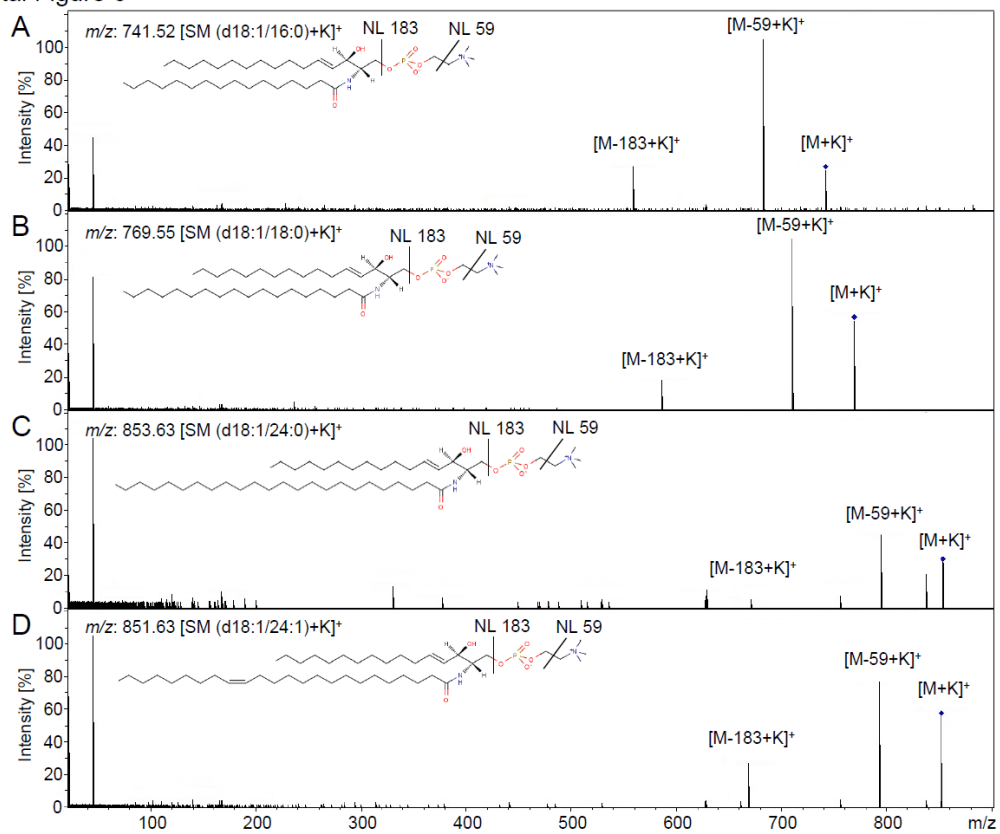
Supplemental Figure 4



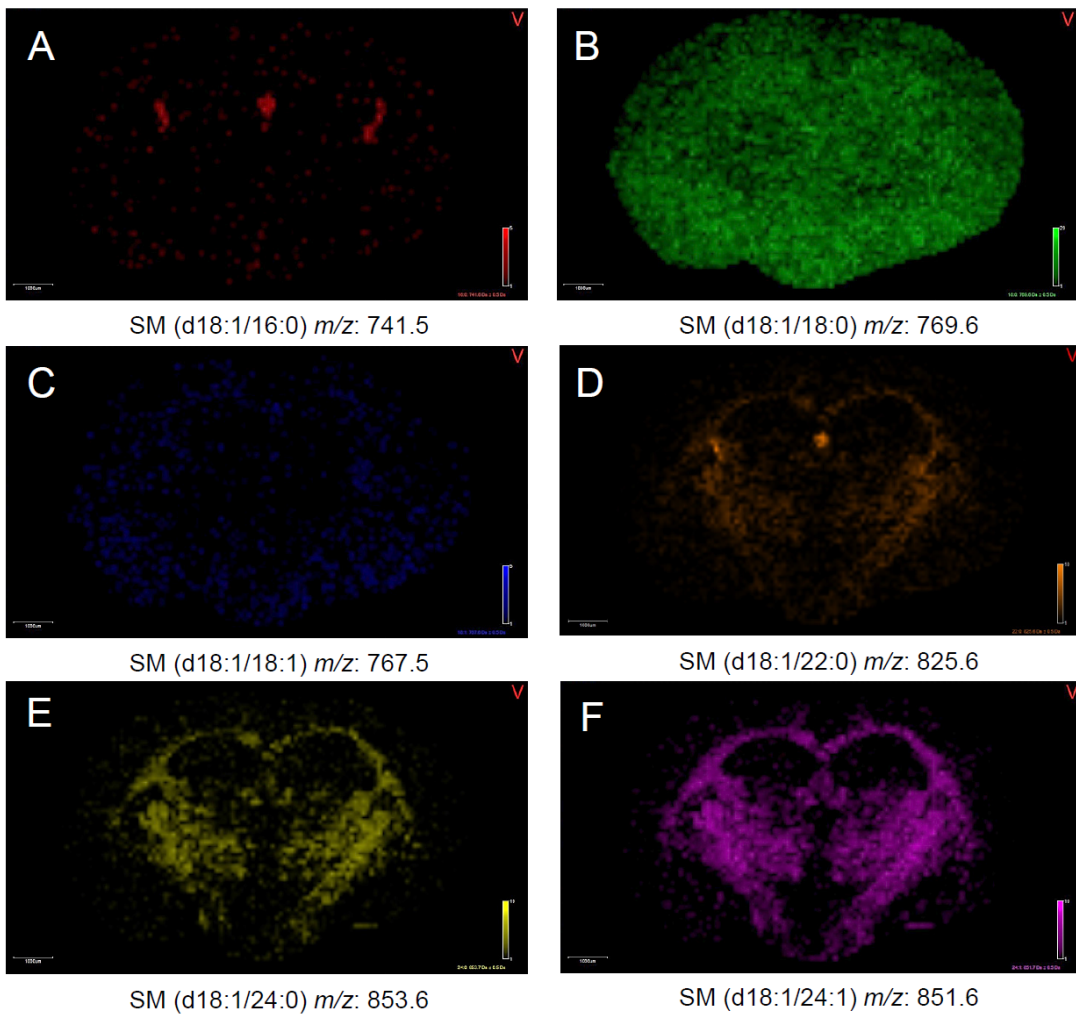
## Supplemental Figure 5



Supplemental Figure 6



## Supplemental Figure 7



### Supplemental Figure 8

